The Pennsylvania State University

The Graduate School

IMPROVING RESIDUAL STRESS AND HEAT TRANSFER IN SHAPE MEMORY ALLOY ACTUATION

A Thesis in

Mechanical Engineering

by

Lawrence Bradley

Submitted in Partial Fulfillment
of the Requirements
for the Degree of

Master of Science

May 2023

The thesis of Lawrence Bradley was reviewed and approved by the following:

Aman Haque
Professor of Mechanical Engineering
Thesis Advisor

Jing Du
Associate Professor of Mechanical Engineering

Robert Kunz
Professor of Mechanical Engineering

ABSTRACT

Shape memory alloys (SMA) are a class of functional materials that are best known for their very high strength to weight ratio as actuators. This is due to temperature dependent phase transformation, which allows 4-6% strain. When heated, they contract in length – thereby producing very large actuation force. Despite their unique properties, the applications of shape memory alloys as actuators are limited by (a) slow actuation rate that is critically influenced by cooling time and (b) residual stress in the material that reduce the amount of the recoverable strain. In the first part of this research, we propose a new actuation mode where we integrate conduction mode heat transfer in the SMA wire, without any additional element that increases size of weight of the actuators. This is motivated by the observation that the it is not possible to improve natural convective heat transfer for a given specimen cross-section and that conduction mode is faster than convection. We propose a 'segmented actuation' where instead of heating the entire length of the wire, we piecewise segment it and perform controlled heating. This allows the unheated segment (neighboring two heated ones) act as a temporary heatsink that receives heat by conduction. Using a controller along with segmented heating of the alloy, we demonstrate that the actuation rate can be improved three-fold, without any change in the shape memory properties. However, the segmented approach essentially costs some recoverable strain. In the second part of this research, we focus on the residual stress in the SMA wire, which is difficult to avoid because the wires are manufacturing by drawing process. We propose a unique annealing process that works at significantly lower temperature (<200℃) compared to conventional annealing processes. In this process, we apply very high current pulses (100A) with small pulse width (4 micro-seconds) and low frequency (2 Hz). This unique power application does not allow large accumulation of heat (to raise the temperature), but the electron wind force is very strong to mobilize and eliminate the defects and precipitates. We demonstrate our proposed Electropulse Aging Treatment (EAT) to improve the recoverable strain by 30%, mitigating some of the loss

from segmented heating. Through higher current electropulsing, the phase transformation temperatures can be altered, in addition to improving the recoverable strain, signifying another mechanism in which the actuation rate could be improved. Additional work was done on non-destructive testing methods, where a new method of mapping residual stresses in welded materials was developed. By using the cooling rates at each pixel in the thermal image data of a sample during cooling, defects could be determined through changes in those cooling rates due to changes in heat transfer properties from defect concentrations.

TABLE OF CONTENTS

LIST OF FIGURES

ACKNOWLEDGEMENTS

I would like to start by acknowledging and giving thanks to my advisor, Professor Aman Haque, for his invaluable guidance and unwavering support throughout this research. He was instrumental in guiding the research as well as my writing of this thesis. Without his mentorship the realization of this work would have been unobtainable. I would also like to thank Professor Jing Du for her guidance and exceptional recommendations that significantly improved this thesis. In this paper there is a schematic of the Northrop Electropulser which I would like to thank Logan Sharp for providing. Additionally, I would like to thank Nahid Al-Mamun for running the XRD tests in Chapter 3 and providing that data. Both Logan and Nahid were extraordinarily helpful throughout this research as colleagues.

This research was partially supported by the US National Science Foundation (DMR # 2103928) and a Focused Research Award from Sony USA. Any opinions, findings, and conclusions or recommendations expressed in this material are those of the author and do not necessarily reflect the views of the National Science Foundation or Sony USA.

Chapter 1

Literature Review

Motivation

Shape memory alloys (SMAs) are a class of functional materials. These materials are unique in the fact that they are able to withstand large amounts of recoverable strain. Recoverable strain refers to the strain that the material is able to withstand without permanent deformation. This large recoverable strain lends to their ability to be used in numerous applications. One current application is in the medical field, where they are able to be used as stents [1,2]. Research continues for future medical applications of SMAs, such as reducing the size of endoscopic mechanisms, which has the potential to make endoscopic procedures more pain-free [3,4]. Additionally, these materials have shown promise in the field of Civil Engineering, where researchers have investigated their use as seismic isolation devices [5], or as a construction material to dampen seismic events. [6].

To continue to advance these domains, there are several key improvements that need to be made in the shape memory properties of shape memory alloys. An important property to improve is the strength of the material, which is important for civil applications and actuator applications [7]. Despite having a magnitude or so more recoverable strain than conventional alloys, actuator applications can be improved through even greater recoverable strain [8].

The final and most important improvement to SMAs will come in the form of improved functional fatigue life [9]. Functional fatigue is an important property to improve because it is reached quickly in shape memory alloys [10]. Improving this will allow SMAs to be used in high frequency/high cycle applications. However, in order to improve these properties researchers

must continue to iteratively improve SMAs. The work contained in this paper is an attempt to further improve these properties through novel heat treatment and actuation methods.

Shape Memory Alloy Background

Shape memory alloys are a class of functional materials that are able to recover large amounts of strain (greater than 6%). This large recoverable strain leads to quite a few applications for the material, one of is actuators. Commercial SMAs generally are made from NiTi, but they can come in a number of compositions such as Copper based [11] and Iron based [12]. Generally, these other varieties of SMAs are researched since they are a lower cost alternative to NiTi. However, this reduction in cost often results in reduced shape memory properties, highlighting the need to further improve them.

SMAs are unique because they can recover a large amount of strain in comparison to other metals. Their ability to recover large amounts of strain is cause by the martensitic transformation, which occurs in the presence of stress or heat. This transformation is what gives the SMA its ability to recover large deformations. This transformation is characterized by the change from the parent phase, austenite, to the martensitic phase [13]. Generally, the material starts in a twinned martensite phase. The application of strain causes a detwinning of the martensite, leading to a detwinned martensite. Then, through heating, the strain is recovered as the phase shifts towards the austenitic parent phase [14]. Since the parent phase of the transformation is the end phase, we refer to this as the reverse martensitic transformation. According to Moraweic et al [15] the transformation has an intermediate phase, referred to as the R-phase. The R-phase is present when the martensite is detwinned from the application of stress. Following the intermediate phase, we have a transition to parent B2 austenite [15]. The forward martensitic transformation of course would be the opposite of this transformation.

The reverse martensitic transformation is characterized by four temperatures; Martensite Start (M_s), Martensite Final (M_f), Austenite Start (A_s) and Austenite Final (A_f) [16, 17]. The recovery of the strain, which is useful in actuation applications, begins to occur at the A_s temperature, and finishes by the A_f temperature [18]. This heating to A_f is referred to as a temperature induced transformation, as the increase in temperature is what leads to this transformation. In between these temperatures, the two phases are both present, with the austenite phase increasing with temperature [19]. In addition to thermally induced transformations, SMAs undergo stress induced transformations during the beginning of the reverse martensitic transformation. The initial loading or stress on the SMA in the martensitic phase results in the intermediate R-phase [20].

SMAs are commonly researched in actuation applications because they possess certain qualities that other actuators lack. First, they are solid state actuators and therefore light weight [21]. The solid-state nature of SMAs means that only the SMA is required to make an actuator, this lack of parts reduces the weight considerably in comparison to electric motors. This solid-state nature has other benefits, however. Their small size is an additionally beneficial trait, making them more compact that other actuators in many applications, with a high strength to weight ratio [4,21].

Despite the benefits of using SMAs as actuators, they have certain shortcomings that preclude them from being used as actuators in many applications. The primary issue is their short functional fatigue life, which refers to the point where shape memory alloys begin to lose these functional properties [3,4]. According to Eggeler et al, functional fatigue is different from structural fatigue in the fact that it does not mean the mechanical failure of the material, but rather indicated the functional failure of the material – the loss of shape memory properties [22]. This functional fatigue is an issue in SMAs because it occurs from thermomechanical cycling of the material, as known as actuation. Depending on the load and strain on the material, the SMA can

begin to exhibit functional fatigue in 1000 cycles, which is low for most actuator applications [23].

SMAs suffer from other shortcomings such as a low displacement, actuation speed, and non-linear control [24]. The low displacement issue is a bit of a misnomer – SMAs have a unusually high recoverable strain, however improving this recoverable strain makes them useful for more applications [25]. Researchers have been working for the past decade to improve the shape memory properties, using a variety of methods such as thermomechanical treatment [26] and using different alloys [27, 28]. Typically, SMAs (NiTi) will have a recoverable strain in the region of about 6%.

Huang et al was an earlier researcher on the thermomechanical treatment of SMAs, looking at how annealing effected the super elastic properties [29]. Huang found that the recoverable strain can be improved through annealing and transition temperatures can be adjusted. The addition of alloying elements to NiTi has also been investigated to improve shape memory properties. The addition of a third alloying element has been shown to improve the properties of shape memory alloys [30]. Salvetr et al researched the addition of several different elements to the NiTi composition, and found a that it can be a way to mitigate undesirable phases in the structure [31]. These two methods of thermomechanical treatment and the addition of alloying methods are a common way to improve the shape memory properties.

Additionally, the slow actuation rate of SMAs is another issue, as faster actuators are desirable [32]. The actuation speed of SMAs is generally far lower than that of other types of actuators [24]. To improve the actuation speed, researchers typically will either reduce the size of the actuator [33] or utilize a non-axial method of actuation [34]. Though these two methods works, it is not ideal for actuation applications because reducing the diameter reduces the useful load of the actuator, and using non-axial methods reduce the recoverable strain. Increasing

actuation frequency while maximizing recoverable strain and the useful load is the best way to improve the actuation of SMAs.

A large problem with using SMAs as actuators is the control of actuation. The control of SMA actuators is difficult because the martensitic phase transformation that give the materials their shape memory properties is nonlinear in nature [24]. In addition to being nonlinear, precise control can be hard to repeat, requiring a feedback loop for accurate control [35]. These feedback loops can eliminate some of the control issues with SMA actuators, but at the cost of making what is supposed to be a simple actuator more complex.

Though research continues on the use of SMAs as actuators, research on the material properties, or more importantly, the shape memory properties of SMAs tends to be the primary focus of the literature. Though increasing the ability of SMAs to be used as actuators is important, this can be done from a more fundamental standpoint by improving the shape memory properties. These can be improved thermomechanical treatments [36] and changes in alloying elements [11].

Gap In Literature

The literature on improving the recoverable strain and functional fatigue life is filled with various methods for improving the shape memory properties, such as adding alloying elements [27] or using thermomechanical treatments [37]. Ideally, new versions of these two methods need to be introduced, as further improvement of shape memory properties is ideal. The new methods need to improve the shape memory properties even further than the methods in the current literature. The cost and complexity of these methods should also be considered, as reducing the cost of the material could increase potential applications.

Additionally, the literature tends to have gaps on actuation methods in order to improve actuation frequency of SMA actuators. Most of the literature tends to focus on the

thermomechanical treatments as a means to improve shape memory properties [11] and in turn the actuation frequency, or through actuation methods that likely lead to poor actuators for larger loading conditions [28]. To continue to improve the actuation frequency of SMAs, new methods need to be developed that have not yet been considered. These methods should improve the actuation frequency by several factors when compared to conventional methods. The purpose of this work is to discover and investigate novel methods of improving these shape memory actuators

Chapter 2

Increasing Actuation Rate

Introduction on SMA Actuation

A limiting factor of SMA actuation frequency is fatigue. It was found by Motemani et al that cooling at too quick of a rate can decrease the fatigue life of the alloy and lead to mechanical failure [38]. To confirm how quickly our SMA was cooling compared to the methods outlined in that paper, experimental data was compared to modeling of how quickly SMAs will cool under forced air induction and water cooling, both of which lead to fatigue problems. Figure 2-1 shows the results of this modeling, with the experimental cooling rate closely reflecting the modeling of natural air convection, validating the model. From the model, it is assumed that only small increases in actuation rate can be achieved before structural fatigue becomes an issue.

The modeling was completed in MATLAB, where the surface temperature of the alloy was iteratively calculated at each second of cooling. The starting temperature was 60 ℃, representing the start of the martensitic transformation. The modeling was stopped at 18 seconds, the time it took for the martensitic transformation to be completed in the experimental data. The modeling differences between the models is that the value of the convective heat transfer coefficient (h) was varied for each situation. The heat transfer coefficients for water cooling, forced convection, and natural convection were 120, 60, and 20 respectively. These values of the heat transfer coefficients are estimated values within the ranges for those modes of heat transfer, not specific values.

The modeling was based on several elementary heat transfer equations. Equation 1 is the convective heat transfer equation, which is used to calculate the heat transfer rate (Q) at a given surface temperature (Ts). This heat flux is used with equation 2 to find the new surface temperature (T), which is then used to iteratively find the next heat flux. The other terms in these

equations are the surface area (A), m is the mass of the sample (can vary with surface area), and c_p is the specific heat of nitinol (0.32).

$$\text{Eq 1: } Q = h*A*(T_s(i)-T(i))$$

$$\text{Eq 2: } T_s(i) = T_s(i-1) - (Q(i-1))*(1/(m*c_p))$$

These equations are used to calculate the surface temperature of an SMA sample at each second of the cooling process. In the case of Figure 2-1, we are specifically modeling the cooling of a 500-micron SMA sample over the course of 18 seconds. It is found that the experimental data is similar to the modeling data, however not exact. The discrepancy is likely due to factors such as an estimated heat convection coefficient, constant heat transfer properties, and a idealized material properties. What the modeling tells us is that to get significant cooling rate gains, we would need to use cooling methods that have been shown to be detrimental to SMA properties [38]. The purpose of these results being in this introduction is that this modeling had significant influence on the research and experiments that were conducted in this chapter. These preliminary results showed us that increasing the heat transfer through the material would likely be a poor method of increasing the actuation frequency.

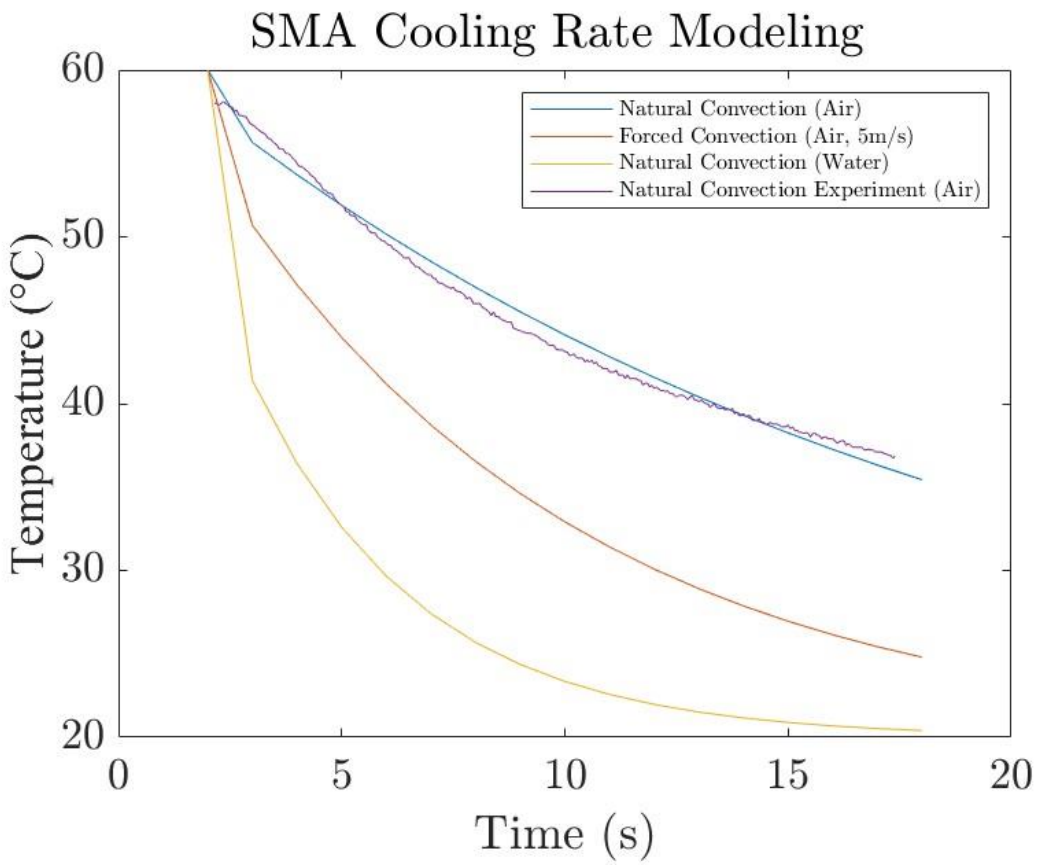

Figure 2-1: Experimental SMA cooling data versus modeling of cooling in different conditions.

However, increasing the cooling rate of the shape memory alloy during actuation is not the only method of increasing the frequency. The type of alloy and the method in which it is actuated can be used to further increase the actuation frequency. It has been shown that decreasing the size of the SMA to increase the surface area in proportion to the volume of the sample can be used to increase the cooling rate (such as thin film actuators) [39]; however, this may lead to the same fatigue issues [38]. Figure 2-2 shows a small experiment in which three different diameter SMAs were actuated conventionally, to compare the rate of actuation. It is found, as the current literature had suggested, that the thinner wires will actuate faster (the thinnest wire data has some small clipping issues, do to it actuating faster than the sensor's sampling rate could handle). The 0.5mm wire is the best middle ground for increasing actuation

rate, while not sacrificing too much strength or cooling too quickly, and was therefore used for the experiments in this and subsequent chapters.

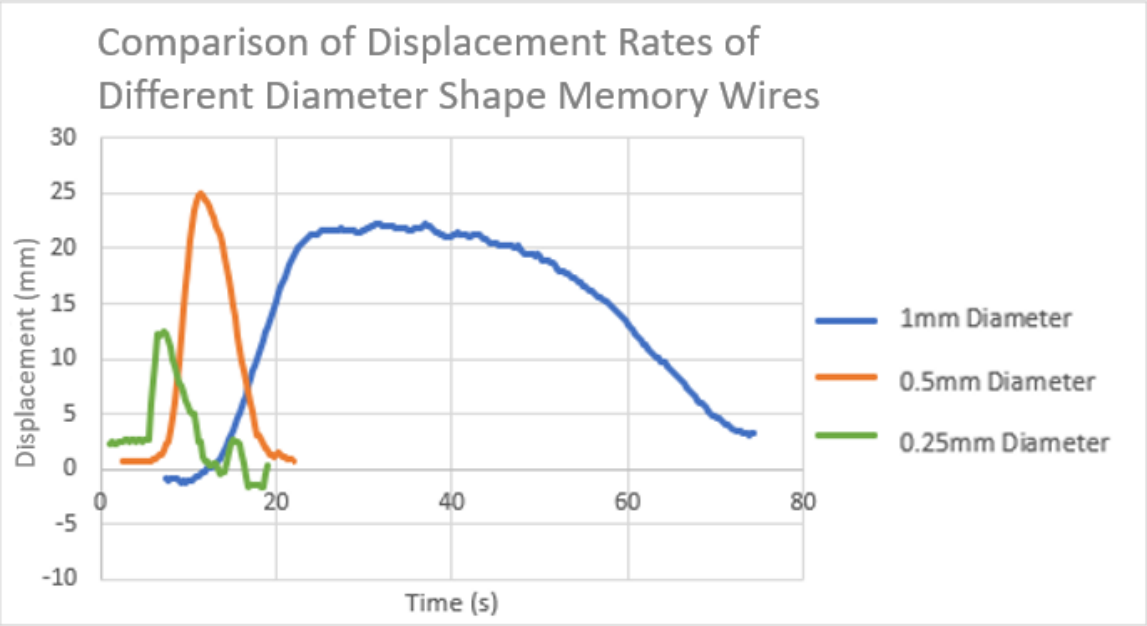

Figure 2-2: Comparison of actuation rates of different diameter SMA wires.

Another option is to use a different actuation method, such as a bending actuation rather than axial actuation [34]. Those two methods have both be investigated deeply; however, to further increase the frequency it is necessary to think of alternative methods of actuation. A novel method of doing this is referred to as segmented actuation, which involves heating and cooling sections of the SMA independently. Conversely, all current methods of SMA actuation involve heating the entire length of the alloys at once. Segmented actuation is unique in the fact that a single SMA specimen is treated as if it is several separate samples. Figure 2-3 outlines how this method works.

As shown in the figure, there are two segments of the specimen which are heated and cooled independently; however, the number of segments can be increased. In the two-segment

example, actuation begins with both segments in their cooled, pre-strained original states. The first segment is then heated until all of the strain is recovered, and then it is allowed to cool. However, conventional SMA actuation would allow this wire to cool completely before being heated again, but in this novel method of frequency optimized segmented actuation (FOSA), that is not the case. As the first segment is cooling, the second segment is fully heated before the other can cool and expand the full length. Then, the second segment is allowed to cool, and as it is cooling the first segment is heated again, despite not yet fully cooling and expanding. In this method, neither segment is able to fully cool. The reason for not allowing it to fully cool is that the cooling part of the actuation takes significantly longer than the heating, and by eliminating some of this cooling the actuation rate can be significantly increased at the cost of a lower recoverable strain.

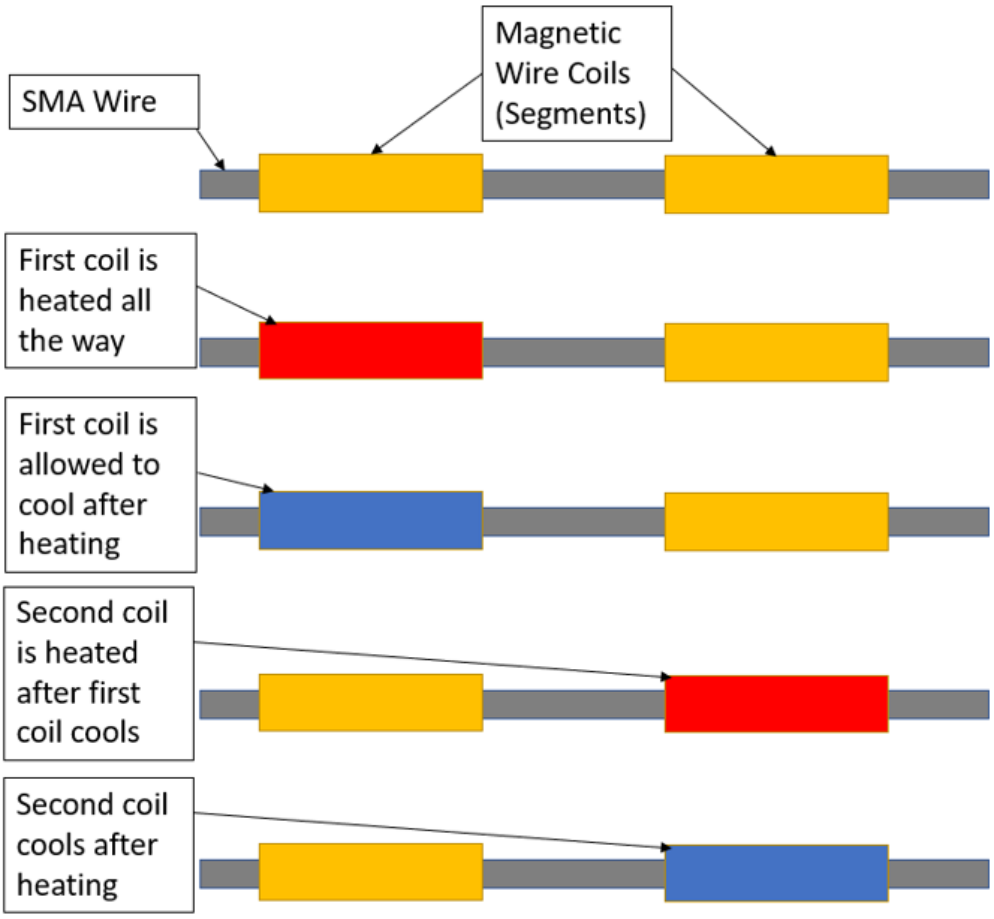

Figure 2-3: Operating principle of segmented actuation.

Methods

Materials

In this experiment, commercially available NiTi wire was used to create the samples. Commercial NiTi is generally an equiatomic composition of Ni and Ti, as per the manufacturer, Kellogg's Research Labs. Conventionally, the samples would be heated using Joule heating; however, these samples were heated using a different method which involved wrapping magnetic wire around each segment and passing current through this magnetic wire. This method of heating relies on the conduction of heat from the magnetic wire into the SMA; however, it was found through testing that this method results in slightly faster heating and was therefore preferred. The magnetic wire was 32 AWG enamel coated copper wire.

A 30cm long sample of 500-micron SMA was used, with each magnetic wire segment being 25cm long. This method of actuation the SMA wire was used in all subsequent experiments in this paper. For the segmented actuation and the frequency optimized segmented actuation, 60 cm of SMA wire was wrapped with two coils, each 25cm in length, using the same 32AWG magnetic wire. Since the magnet wire is enamel coated, the coating was removed with a butane lighter on the ends of each coil to allow current to be passed through the coil. The actuation temperature of the SMA wire (A_f temperature) was 80℃.

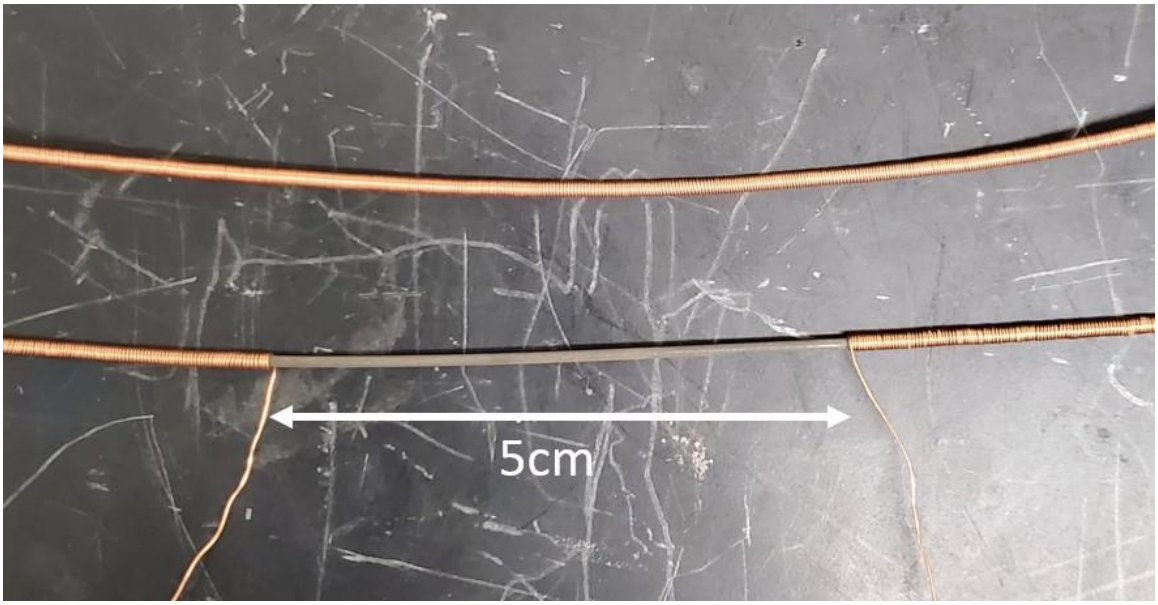

Figure 2-4: Coiled conventional SMA sample (top) along with a coiled segmented sample (bottom). Note that in between the coiled segments is a 5cm gap.

Segmented Actuation

As seen in applications such as computer chips, one method of increasing the cooling of a material is the addition of a heat sink. One of the primary advantages of SMA wires is that they are light weight, therefore it is unwise to add large and presumably heat sinks to the wire. However, some of the SMA wire itself may be used as the heat sink. This can be done by having a region in the center of the wire that is not used for actuation, but is used to conduct heat away from the sections that are used for actuation, as seen in figure blank.

To test that this will improve the actuation rate of the SMA, two samples were constructed. One sample was a conventionally actuated SMA wire, with one single 50cm coil of magnetic wire. This sample is actuated by passing current through the single coil, and then allowing it to fully cool after contraction. The second sample is constructed using two coils of 25cm each, as can be seen along with the conventional sample in figure 2-3. Between these two

coils is a section of unactuated SMA wire that is 5cm in length, which will be acting as our heat sink. It has been shown that this heat sink offers a slight increase in the actuation rate of the SMA, therefore it was used for all of the segmented tests at the request of the sponsor.

Frequency Optimized Segmented Actuation

Once the samples were completed for the FOSA experiment, the samples were loaded into the displacement testing jig (appendix A). The displacement testing jig incorporates and ultrasonic sensor which records the displacement of the sample during actuation. The goal is to see how quickly the FOSA sample is able to actuate in comparison to a conventionally actuated SMA wire, which in our case is a SMA wire with a single 25cm long coil. Each sample is loaded into the displacement testing jig and is actuated for several cycles to see how quickly it is able to actuate. In the case of the FOSA sample, it is not allowed to fully cool during actuation, and has power delivery controlled via an Arduino Uno based controller. This controller (appendix A), is used to send power to each coil for a specified amount of time. The time power is sent to each coil was determined through trial and error, finding which time frame resulted in the fastest actuation rate.

Results and Discussion

Segmented Actuation

The response of the conventional sample and the segmented sample are show in figures blank a and blank b. Figure 2-4a shows that we achieve an average of 34 seconds cooling time for each cycle, while figure 2-4b shows an average of 26 seconds to cool. This difference results in the ability to complete four cycles of segmented actuation for every cycle of conventionally actuated SMA. It is theorized that this increase in cooling rate is the result of the heat sink centered between the coils of the segmented sample. Despite the gap being a fraction of the size

of the coils, it is able to conduct enough heat away from the coils to speed up the cooling, or the transition from the austenitic parent phase to a twinned martensitic phase.

The gap between the segments was also investigated. A small experiment was conducted to see how the gap size affected the improvement in the actuation rate. It was found during the experiment that an increase in the size of the gap improved the sample up until about a 5cm wide gap, after which the returns of increasing the gap sized were greatly diminished. This led us to keep the gap at 5cm for these experiments, and it is doubtful that there is any considerable improvement to be had past what we have observed with the 5cm gap.

The one downside to this method is that it requires an increase in size of the sample for a given displacement. Since there are two segments of the wire being used to actuate the SMA, each one needs to be able to fully actuate the alloy, resulting in a sample that is double the length compared to conventional samples. The tradeoff is that the sample must double in size, or the displacement during actuation must be halved. In applications where an increase in actuation rate is the primary concern, this may be a worthwhile tradeoff; however, it may create issues in applications where high displacement is the desired characteristic. Mechanical amplification of the displacement may be a method of mitigating this tradeoff, however the practicality of this has yet to be investigated.

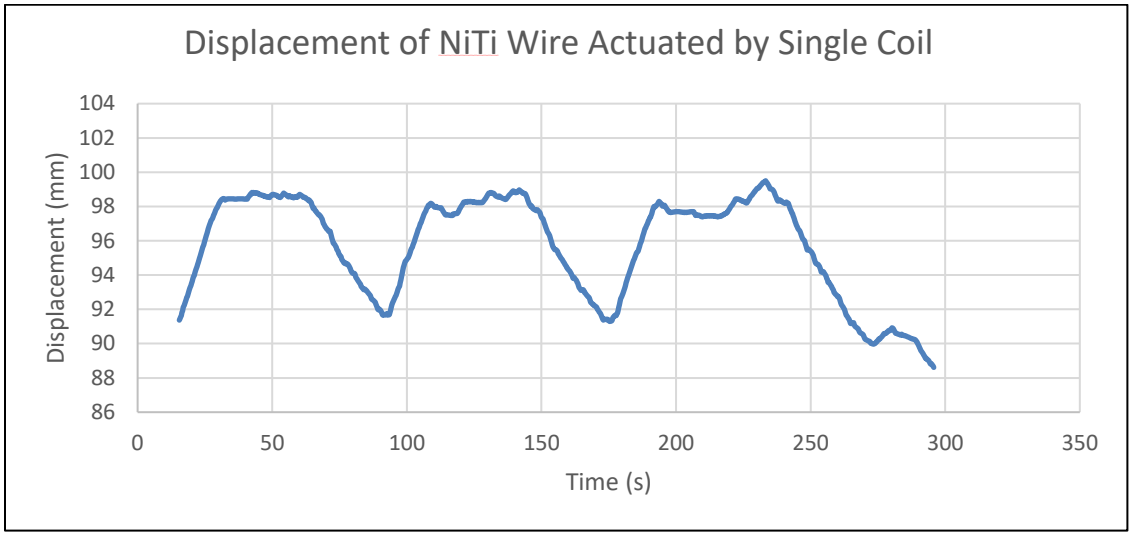

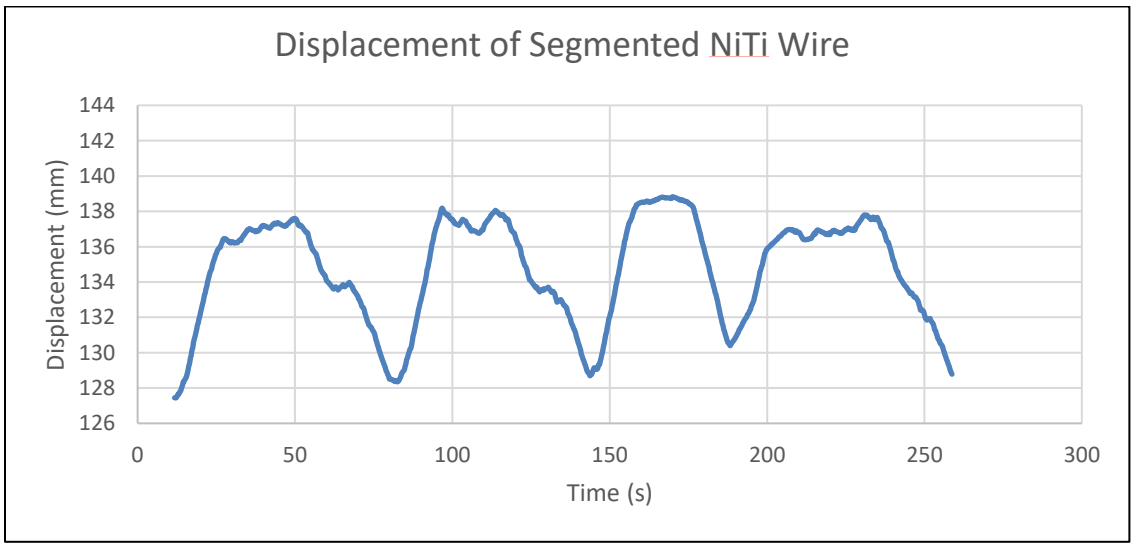

Figure 2-5: Figure 2-5a (top) shows the response of the conventionally actuated NiTi wire. Figure 2-5b (bottom), shows the response of the segmented NiTi wire.

Frequency Optimized Segmented Actuation

The addition of a controller to dictate the delivery of power to the segments allows for a further increase in the actuation rate of the SMA wire. In pervious experiments, power was sent to a single coil from the DC power supply. Once power was turned off, the DC power supply was connected to the 2nd coil, and once the first was fully cooled, the 2nd coil was powered. It was hypothesized that by using a device to control the power delivery to the coils, the actuation rate may be further increased. It was found that the SMA wire had roughly a 300% increase in actuation rate in comparison to the conventionally actuated sample, and that the SMA wire actuated 86% faster than the standard segmented sample. Figure 2-6 shows the rate of actuation of the sample, in the form of a time versus displacement chart.

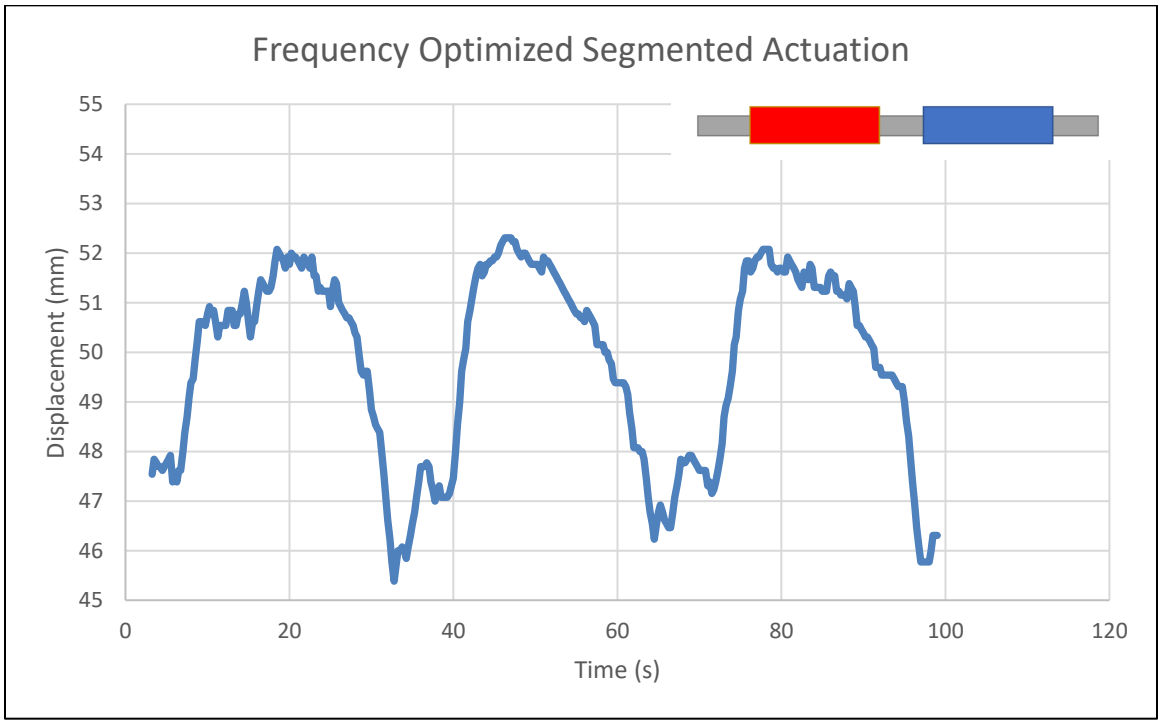

Figure 2-6: Time versus displacement chart of the Frequency Optimized Segmented Actuation sample.

The increase in the actuation rate is achieved at the cost of the displacement, or recoverable strain. The recoverable strain of the FOSA sample is half that of the standard segmented or conventional samples. The loss of recoverable strain is caused by the fact that when using the FOSA method neither segment is allowed to fully cool, resulting in only a partial actuation. By keeping both segments from fully actuating, the sample is forced to operate primarily in the intermediate R-phase, rather than undergoing a full martensitic transformation. Figure 2-7 illustrates this process, which is based on a stress-strain-temperature schematic by Follador et al [74]. The schematic is of the typical response of an SMA undergoing the martensitic transformation in the shape memory effect region. Overlaying the schematic are red lines, which is the path that the sample will be taking during FOSA. This "clipping" of the displacement leads to smaller temperature changes for actuation, resulting in faster actuation.

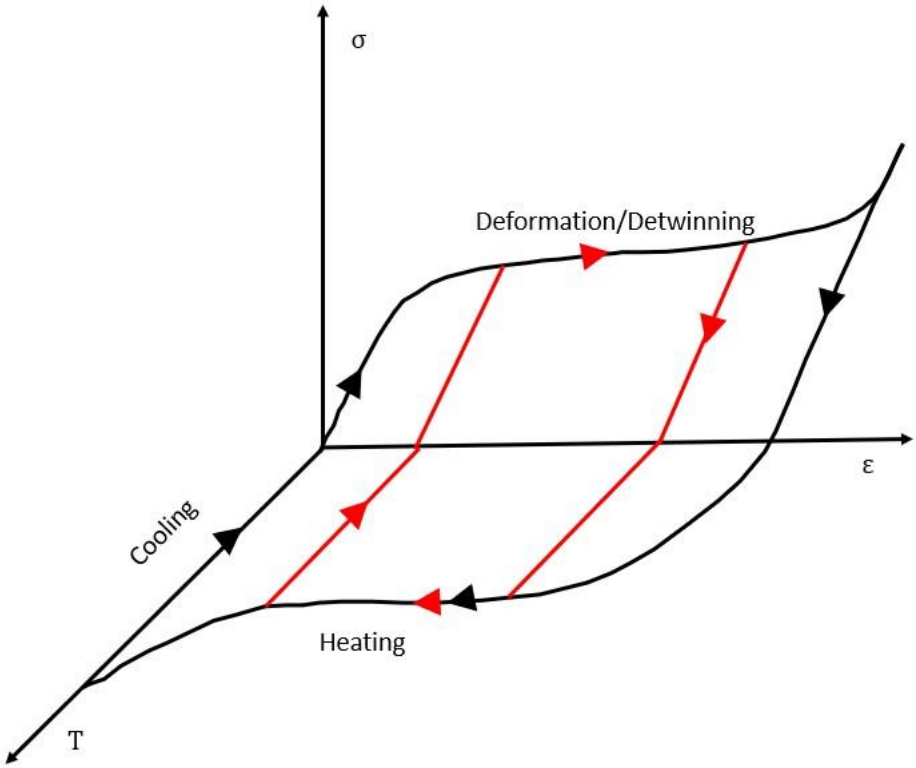

Figure 2-7: Frequency optimized segmented actuation stress-strain-temperature diagram [74].

Conclusion

Increasing the actuation rate of shape memory alloys is challenging due to the physical limitations of the material, specifically the risk of fatigue. When cooled too quickly, shape memory alloys have been shown to have an increase in crack growth resulting in structural fatigue early in the alloy's lifespan. To increase the actuation rate, it is necessary to do so without significantly increasing the rate of cooling of the material. By focusing on novel actuation methods, rather than increasing the rate of heat transfer, the actuation rate of SMAs has been increased. Through the use of segmented actuation, the actuation frequency is increased by 24%. However, additional gains can be made at the cost of the recoverable strain, using the process of frequency optimized segmented actuation. This frequency optimized segmented actuation is able to increase the actuation frequency by 86% when compared to the standard segmented actuated sample. Increasing the actuation rate this significantly comes at the price of the recoverable strain, decreasing the displacement of the sample by 50%.

Improving the recoverable strain, while simultaneously continuing to improve the actuation frequency should be the focus of future work. Improving the actuation frequency can be done easiest by limiting the recoverable strain; however, it is likely that the decrease in the strain shown in this paper is too great for most SMA applications. In fact, for many applications an increase in the recoverable strain is required, therefore finding a balance should be the focus of future work. In the remaining chapters of the thesis, the focus of the work is on just that – improving the recoverable strain.

Chapter 3

Electropulse Aging Treatment

Introduction to Electropulsing

It is known that the shape memory properties of SMAs can be improved through treatment methods such as annealing. These annealing methods have been shown to improve recoverable strain [40] and improve functional fatigue life [41]. Though annealing methods have proven their effectiveness, they are not without their shortcomings. First, the method is not quick, with standard furnace annealing taking between 30 and 60 minutes. Second, further improvement of the shape memory properties is required to increase the applications of SMAs. A new method of improving these shape memory properties utilizes a different type of annealing. This new method is known as electropulse aging treatment (EAT).

EAT is a method similar to furnace annealing regarding the end result, but EAT anneals based on different principles. In furnace annealing, the sample is held at a high temperature for a long period of time, whereas EAT is a quick process that involves pulsing high current through the material. This pulsing is often sort and quick, with high rise and fall times. The current from the pulse can be anywhere from 100A to several thousand amps, and the pulse width ranges from the lower end of the millisecond scale to the microscale. Additionally, these pulses can be sent through the sample at a number of different frequencies, depending on the pulse width of the signal. Rather than taking an hour in a furnace, a sample may be treated using EAT in 120 seconds. In addition, due to the short pulse width, the sample stays at a much lower temperature during EAT when compared to furnace annealing, making it safer.

Methods

To conduct this experiment, three commercial NiTi samples were used. These samples were 500 microns in diameter with a length of 50cm and had a listed A_f temperature of 80°C. These wires were furnace annealed by the manufacturer; however, one of them was furnace annealed again to attempt to further improve it. Though the first sample was annealed again, the second sample was left in its commercial condition, and the third was used for the EAT. The EAT parameters were as follows; 4ms pulse width, 2Hz, and 100A of current. These parameters were found to be the best available after testing a variety of different variables.

The samples were then placed inside the displacement testing jig, with the Optris PI640 thermal camera recording the surface temperature of the sample. The displacement of the sample was recorded using the Arduino board paired with the ultrasonic sensor. Each sample was loaded with 5 Kg of mass, and then fully displaced by passing 25W of DC current through the sample. The displacement and surface temperature throughout the displacement were then recorded. This was repeated for all three samples.

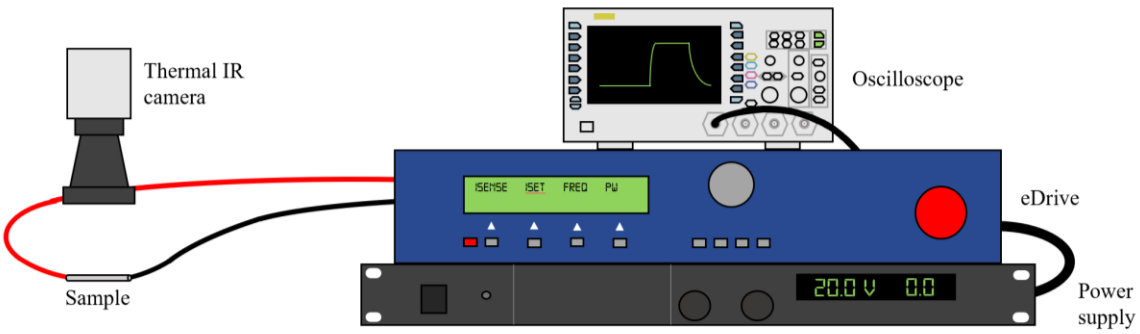

Figure 3-1: Schematic of Northrop Electropulser (courtesy of Logan Sharp).

Results and Discussion

The electropulsing experiments were conducted using the Northrop electropulser, which was capable of delivering 100A of current. Three parameters could be varied in these experiments – the pulse width, the frequency, and the amplitude (current). With so many different combinations, samples were initially tested by measuring the change in resistance after pulsing. This was a quick check to quantitatively evaluate how the samples may have changed during the pulsing, and allowed for different parameters to be quickly tested. It was found through these tests that the best results occurred with the maximum amplitude of 100A, the maximum pulse width of 4ms, and the lowest frequency of 2Hz.

The primary method of characterizing the change in bulk scale shape memory properties was to record changes in recoverable strain of the SMA. This data was obtained by using the displacement testing jig (appendix A), which uses an ultrasonic sensor to record changes in displacement. The electropulsed sample and the conventional sample were both loaded into the displacement jig and actuated for several cycles. The results of this test are shown in figure blank. The results show that the electropulsed SMA wire achieves a roughly 30% increase in recoverable strain when compared to the conventional sample. The plot shows displacement versus temperature to highlight that there is little change in the transition temperatures of the sample after electropulsing. However, it is conceivable that this method could be used to alter phase transformation temperatures such as conventional furnace annealing methods, although this has not yet been investigated.

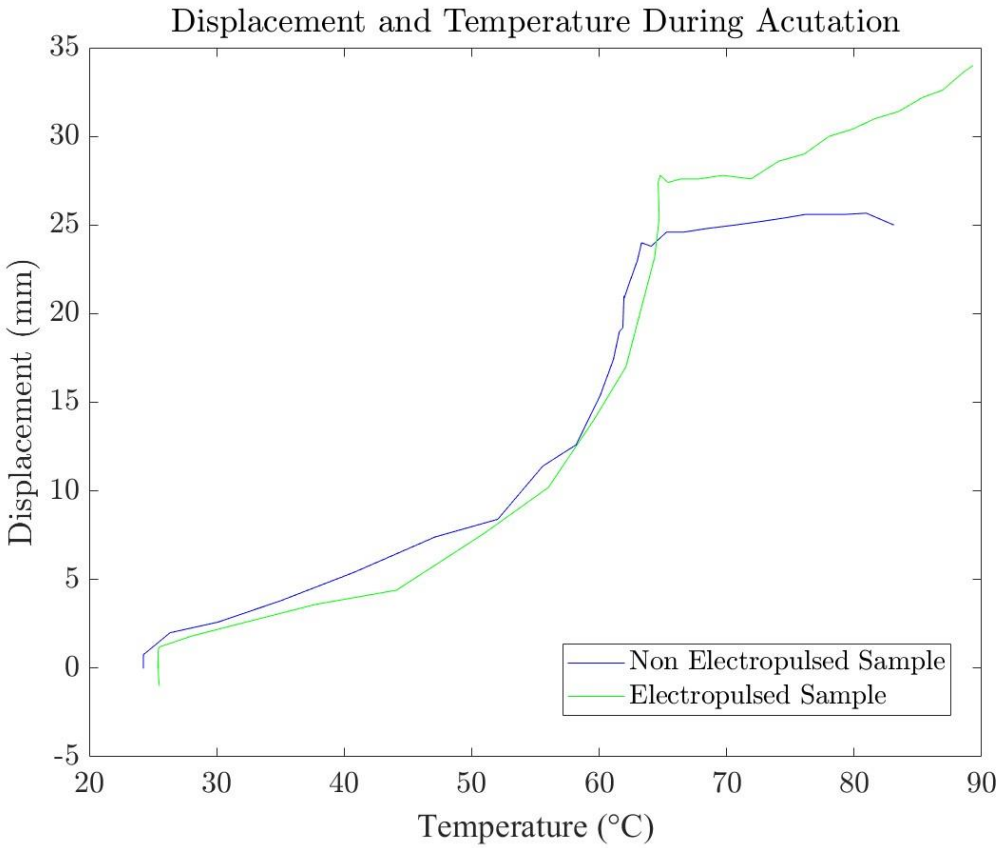

Figure 3-2: Displacement versus temperature chart comparing the bulk scale shape memory properties of the electropulsed sample.

To better understand this change in the recoverable strain, an investigation into the microstructural changes was investigated. To do this, X-Ray Diffraction (XRD) methods were used to characterize the microstructure and presence of precipitates in the conventional sample and the electropulsed sample. Figures 3-3a and 3-3b show the XRD data. As can be seen, in the electropulsed sample there appears to be a decrease in the precipitates, resulting in a stronger martensitic transformation. We theorize that the electropulsing process results in a reduction or shrinking of precipitates in the microstructure, which results in easier plate growth during phase transformation, resulting in the improved martensitic transformation. Further investigation

should be focused on understanding and characterizing the background mechanisms behind the improvement in the bulk scale shape memory properties.

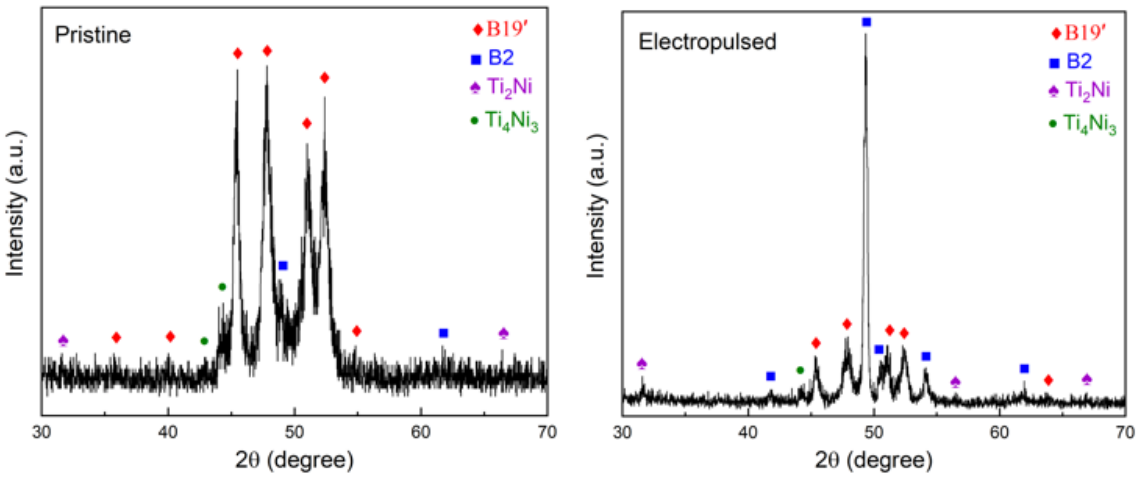

Figure 3-3: Figure 3-3a (left) shows the XRD results of the conventional (pristine) sample, and figure 3-3b (right) shows the XRD results of the electropulsed sample. (Courtesy of Nahid Al-Mamun)

An issue with the XRD results is that it appears that one is showing the martensite phase, while the other sample appears to be in the austenite phase (B19' and B2, respectively). In theory, the sample should both be in mostly the martensitic phase with small pockets of austenite and precipitates, but this is not what is being observed. There are several possibilities for what may be causing this issue. One is an issue in running XRD on these samples. They are thin in diameter and unique being a functional material, so it is possible that the parameters were not correct for testing. The other is that through accidental applied stress (bending) or heat from the XRD process one of the samples underwent a phase transformation – skewing the results. It should also be noted that from the drawing process the wires go through at the factory, that there may be some residual stress induced martensite. It is likely a good idea in the future for pristine samples

to be actuated a few times, along with the electropulsed sample to insure that they are in the same phase.

Conclusion

The Electropulse Aging Treatment method is a way to improve the shape memory properties of shape memory alloys by pulsing short bursts of high current through the material. The improvements from these pulses appear to increase with the amplitude of the current pulse, with the best improvements being seen at a amplitude of 100A. With the 100A of current, and a frequency of 2Hz at a 4ms pulse width, the recoverable strain of the SMA wire improved by 30%. The recoverable strain increased from 5% to nearly 7%. Improvements of the bulk scale shape memory properties were validated by an investigation into microstructural changes in the part, with an observable reduction in precipitates, leading to a more complete phase transformation. The maximum current used in these experiments was 100A, a limitation set by the capabilities of the lab equipment. It can be hypothesized that a further increase in current density may lead to further improvements of the recoverable strain and shape memory properties. Other future work should be focused on further characterizing bulk shape properties, microstructural changes, and the underlying mechanisms resulting in the improvements from this process.

Chapter 4

High Current Electropulse Aging Treatment

Problems with low current electropulsing

Previous experiments involving electropulsing shape memory alloys used a current of 100A or less to treat the alloys. This limitation in the current amplitude was a result of the available equipment, which at most could provide a current of 100A, often times less depending on the resistance of the sample. For our 500-micron SMA samples, this resulted in a current density of 500A/mm^2, which is less than has been found to be optimal in other electropulsing applications. The biggest improvements in the bulk scale properties of the shape memory alloy occur when the material is treated with the highest available current pulses, so it can be theorized that further increasing the current will result in additional gains.

Late in this research, the lab obtained new electro pulsing equipment; the Eagle Harbor Power Module (EHPM). The EHMP allows for currents up to 6000A at a rated 600V; however, it is generally not possible to achieve both of these extremes simultaneously. Regardless, this pulser is able to provide significantly higher current densities than previous equipment, so the goal was to use it to further improve shape memory properties. Due to the success from previous experiments utilizing lesser equipment, it was determined that similar experiments should be conducted with the new equipment.

Methods

The experimental set up for the EHPM is different than the Northrop pulser. The EHMP does not contain an internal signal generator, and therefore relies on an external one to control the signal. The external signal generator is responsible for controlling the pulse width and frequency of the signal being sent to the power module. Another stark difference from the previous pulser is that this set up does not have a direct way to set the current amplitude. Rather, a current monitor is used to measure the outputted current amplitude. This amplitude is then controlled through a combination of pulse width, frequency, an the input voltage from the DC power supply.

Figure 4-1 shows this set up with each component labeled. The entirety of the set up is composed of the EHPM, the DC power supply, the signal generator, the FT-1 (see appendix), the current monitor, and an oscilloscope. There are two important things with this set up that may not be evident from the picture. The first is that the signal generator must be placed at least five feet away from the EHPM during operation, as the equipment lacks proper shielding to be placed in close vicinity. The second is that the FT-1 must be powered on before any signal is passed through it. Failure to apply power to the FT-1 before use may result in damage.

Despite the differences in the pulser, the experiment was conducted similar to that of Chapter 3. For this experiment two samples were created, both from 500-micron-80℃ NiTi samples. One sample was kept in its original commercial condition, and the other was pulsed using the EHPM. The samples were then actuated for several cycles in the displacement testing jig to measure the recoverable strain.

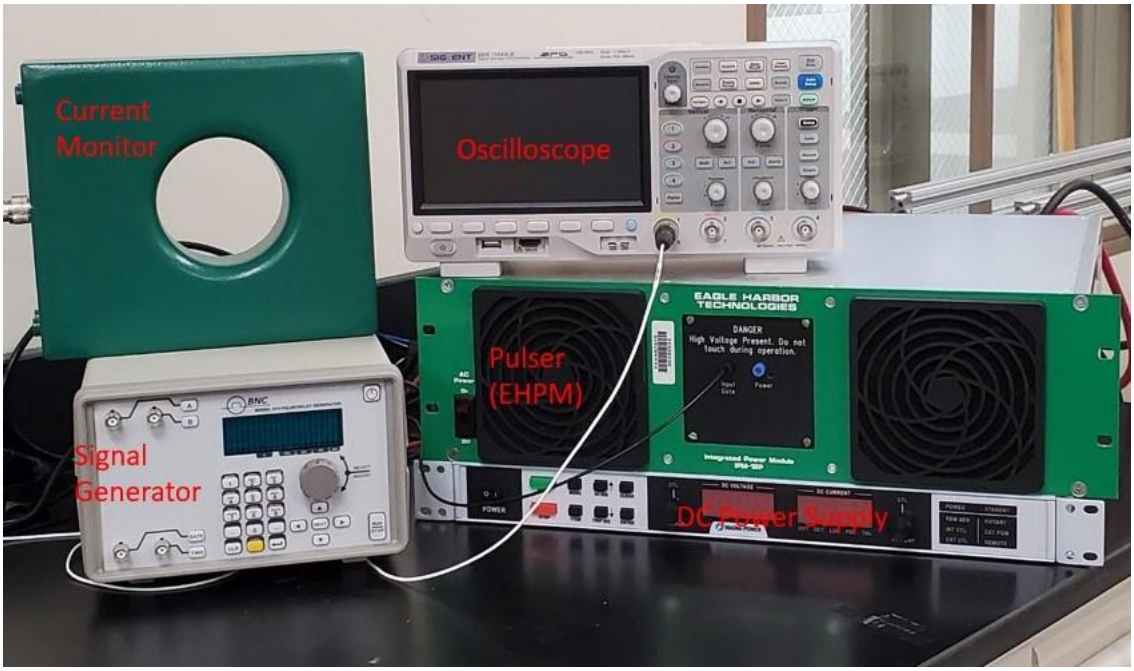

Figure 4-1: Eagle Harbor Power Module.

Results

The recoverable strain of the commercial and the electropulsed sample are compared in figure 4-1. This figure also contains the low current electropulsed sample from Chapter 3, in order to compare the two pulsing methods. The recoverable strain of the high current sample seems to not be improved any further than it was in the low current electropulsing experiment, however the sample's response had clearly changed. It appears that the sample recovers the full strain over a shorter temperature range than the commercial or low current sample. This indicates that in addition to the increase in recoverable strain, there is a change in the phase transformation temperatures of the alloy.

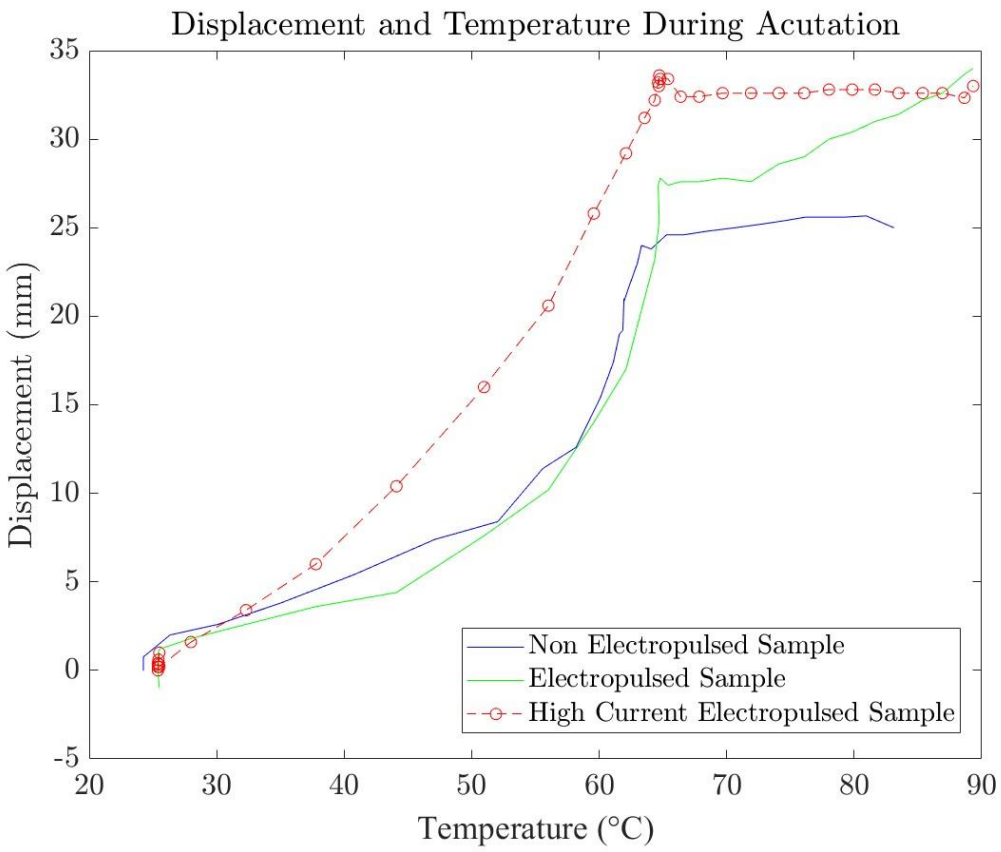

Figure 4-2: Comparison of recoverable strains of different SMA samples. The red sample represents the high current electropulsed sample, the green being the low current electropulsed sample, and the blue representing the as-is commercial sample.

The change in transformation temperature is an improvement over the original transformation temperatures because it allows for the martensitic transformation to occur over a shorter temperature range. This shorter range indicates that the cooling and heating time for the transformation to occur will be shorter, therefore increasing the actuation rate in addition to the recoverable strain. Though the mechanics behind this change are not clear, it is possible that this change is caused by a reduction in the presence of the intermediate R-phase; however, this is yet to be confirmed. Some investigation into the microstructure and underlying mechanism of the

change were performed, however were not able to be completed before the completion of this thesis.

Figure 4-2 shows XRD data of the high current electropulsed sample and XRD data from an as-is commercial sample. The difference in XRD data is not as clear as it was for the low current sample, and it shows possibly a less complete martensitic transformation. However, it is clear that the samples in this case are both in the same phase – indicating that the test was set up better this time. One change was that both of the samples were actuated several times before being sent off for XRD, possibly resulting in the improved results.

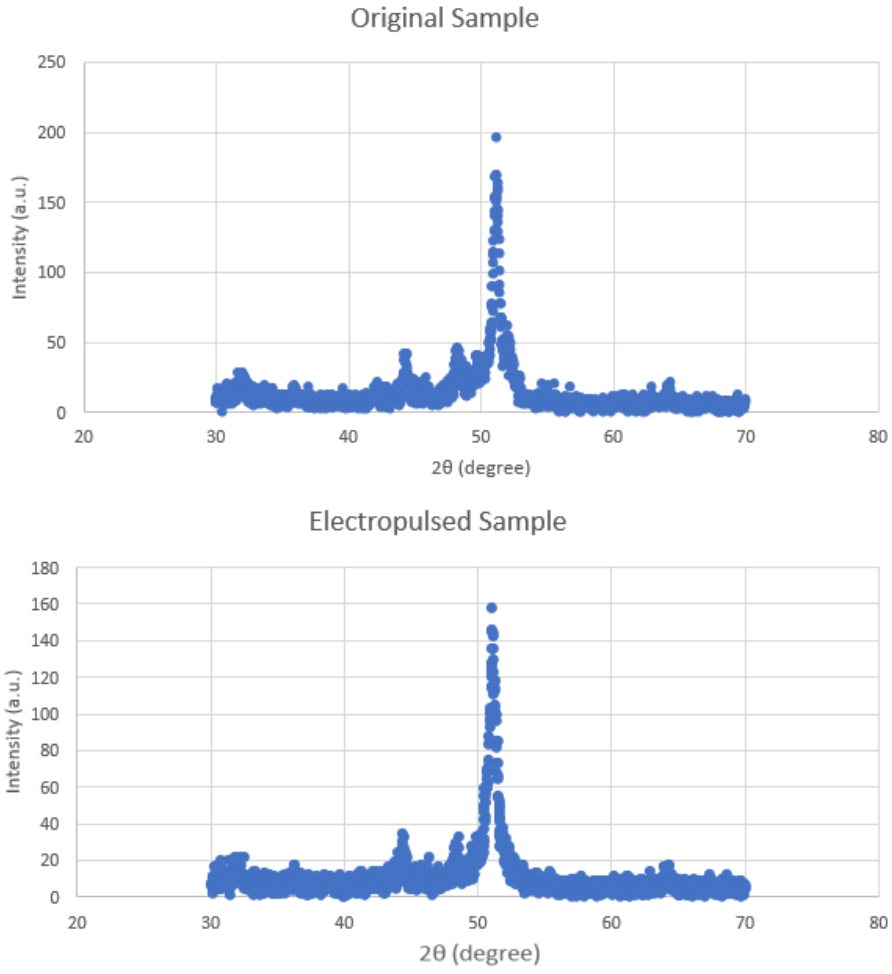

Figure 4-3: XRD results of the original as-is sample (top), and the electropulsed sample (bottom).

To further characterize the changes to the sample, Direct Scanning Colorimetry (DSC) tests were run on both samples, shown in figure 4-3. As with XRD, the results aren't exactly clear. There is little to show phase transformation temperatures are changing, and are not in line with our bulk scale results. The actual response of the DSC results seem to be incorrect as well, as they are showing the phase transformation occurring over a very short temperature range (a few degrees Celsius), which is highly unlikely. In the results for the original sample, there also appears to be a significant amount of noise, which is indicative of poor results. It is possible that these DSC tests were ran incorrectly, and at the time of this thesis we are in discussion with the staff who ran the DSC testing to see how we can improve for future testing. It should be noted that the XRD and DSC results in this chapter were both obtained from the staff at the Millennium Science Complex.

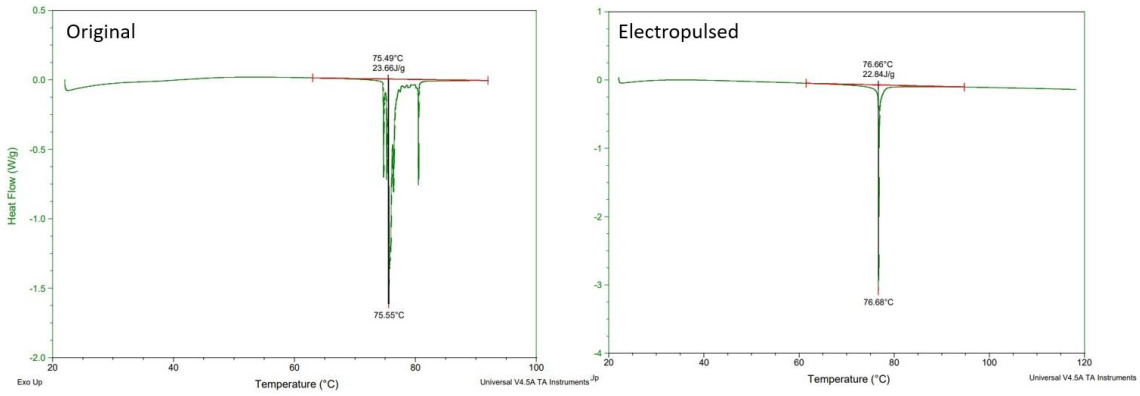

Figure 4-4: High Current Electropulsing DSC results, original as-is sample on the left, electropulsed sample on the right.

Conclusion

The success of improving the bulk scale shape memory properties on NiTi had already been shown using low current electropulsing. Based on that success, it was decided to repeat the

experiments using higher current, to see if the shape memory properties could be further improved. It was found that the increase in current did not lead to an increase in the recoverable strain, however it did change the phase transformation temperatures. The change in martensitic transformation temperatures appears to be a decrease in the temperature difference between M_s and A_f, based on the displacement-temperature charts. Additional methods were attempted to be used to further characterize the changes; however, some issues have occurred in this process and at the time of this thesis, they have yet to be resolved.

Despite the preliminary nature of these results, there is evidence that increasing the current in electropulsing will lead to improved shape memory properties. The change in the transformation temperatures is a favorable one, as raising the M_s temperature, while lowering A_f, will lead to improved actuation times. It should also be noted that the high current sample did have an increase in recoverable strain in comparison to the commercial sample, just not the low current electropulsed sample. It is possible that there are still additional gains to be had in improving the recoverable strain. Due to the large number of possible parameters during electropulsing, it is not reasonable to test all possible combinations, especially in the short time frame given for this high current experiment. With that, only a few dozen parameters were tested during this experiment, out of thousands of possible combinations. Additionally, the current used in this test was around 1000A, but the machine is capable of up to 6000A. Future work should be geared towards maximizing the potential of the EHPM, and further improving the alloy. Additional work should be done on understanding the underlying mechanisms behind the improvement of the alloys during EAT, as well as the changes in microstructure.

Chapter 5

Non-Destructive Evaluation of Residual Stress

Introduction

One thing learned through the shape memory research was that characterizing defect density in a material can be difficult, even in a lab setting. Xray diffraction and Direct Scanning Calorimetry methods proved to be difficult in providing meaningful data on the defects in the sample. A tangentially related piece of work conducted during the early stages of this research is outlined in this chapter. Rather than focusing on the improvement of SMAs, this work focuses on the improvement of techniques to characterize defect density in materials, which is something that we had be aiming to do with diffraction methods on SMAs in previous chapters. However, rather than using SMAs, this research was conducted on welded 316L stainless plates, which tend to be defect heavy in the welded region. The following is on the work conducted in the development of this non-destructive testing method.

Non-equilibrium thermal and/or mechanical processes, such as additive manufacturing or conventional machining, give rise to self-equilibrating stresses in an elastic body even in absence of any external loads [42]. Commonly termed as residual stresses, these are mostly non-uniform fields with magnitude depending on the degree of thermal, mechanical or microstructural (phase) misfit [43]. Accordingly, residual stress may span from sub-grain to few-grain to macroscopic region. Characterization of residual stresses is critical for materials reliability as it is known to alter fatigue and corrosion resistance [44, 45]. Since residual stress increases local hardness, it may decrease both fracture and impact toughness [46]. The exact nature of the stress is very important since tensile stress promotes fatigue crack initiation [47], while the resulting low angle grain boundaries can be microscopically linked to little resistance to crack propagation [48]. Residual stress also leads to Cr depletion in stainless steel, making it vulnerable to corrosion [48]. Stress corrosion cracking is caused by the co-existence of tensile residual stress and chemically

aggressive environment [49]. Compressive residual stress has the opposite effect and is thus sought with various techniques such as laser or shot peening. Since residual stress locally increases the strain energy density, it influences the recrystallization behavior as well [50]. In general, the role of residual stress manifests through the increase or decrease of the mean stress, and the resulting stress redistribution [51]. Even for beneficial contributions of residual stress, a thorough quantitative characterization of the spatial non-uniformity is required [52]. Accurate mapping of residual stress is therefore a vital capability for structural applications.

The motivation for this study comes from the observation that residual stress characterization remains to be a challenging task [53, 54]. Destructive techniques commonly involve removal (hole [55], ring-core [56], crack [57]) of a small volume of stressed material followed by strain (or displacement field) measurement. The challenge is to estimate the stresses in the removed material to the displacement measurements in the adjacent area. The lack of a one-to-one correspondence removed and adjacent materials is reflected in the integral equation, for which an inverse solution is sought. A non-contact version of this methodology replaces the strain gages with electronic speckle pattern interferometry [58]. These are near-surface measurements with single residual stress line profiles. For internal residual stress, the Contour method extracts 2D surface deformation from a newly cut plane to calculate the residual stresses that existed in the component before the cut. Many applications require non-destructive measurements, for which ultrasonic [59] and diffraction (most commonly, X-ray) [60] principles are well developed. However, X-Ray diffraction methods can take hours to complete depending on the sample type, so faster methods are desired. Direct in-operando application of these techniques may be difficult; however, these techniques are very efficient for laboratory environments.

In this study, we explore the application of focal plane array thermal camera or microscopes for residual stress measurement with better spatial resolution, depth-averaging and less cost and sample preparation. A two-dimensional array of many thousands of microbolometers offers up to 12- micron spatial resolution for uncooled (hence cheaper) devices. The mapping is essentially

2D, but can account for significant depth averaging. This is because the thermal penetration depth is a function of thermal loading frequency. For most engineering materials, it can be implemented for a few millimeters [61], which is very suitable for residual stress mapping. In comparison, X-ray diffraction spatial resolution and depth-averaging are about 1 mm and 20 μm respectively [53]. However, there is very little information in the literature connecting thermal imaging to residual stress [62]. Infrared imaging has been demonstrated to detect subsurface cracks in welded materials [63]. Cracks are more readily distinguishable compared to regions of high residual stress, which may not contain even optically discernable voids. Mapping of thermal diffusivity could be a better path towards residual stress, but it requires sophisticated hardware or software-based frequency lock-in algorithms. Thermoelastic stress analysis monitors the small temperature changes in specimens subjected to elastic strain [64]. However, the requirement of mechanical loading may be problematic for non-contact applications of structures during operation (in-operando testing). Another approach is to relate thermal diffusivity to plastic deformation, where increased thermal scattering has been captured in the proximity of failure surfaces of a mechanically loaded specimen [65].

We present a new technique that uses pixel by pixel cooling rate of a surface (previously heated to a uniform temperature) to map regions of different thermal diffusivity. The underlying principle is that regions with high residual stress will have slower cooling rate when compared to areas with little or no residual stress. The mechanistic perspective is that residual stress is accommodated in metals by very high density of defects, such as low angle grain boundaries [66]. Since heat flow in metals is predominantly via electrons, we hypothesize that electron-defect interaction controls heat transfer in a way similar to electrical resistance [67]. For a region with high density of low angle grain boundaries, the electron scattering is significantly higher compared to regions with lower or no defect density. An example of this is the low thermal conductivity of additive manufactured metals and alloys, which can be improved upon annealing [68]. Such high scattering will impede the heat flow, which can be captured with a focal plane array thermal camera, and then evaluate the cooling rate for each pixel of the images. The technique is nondestructive and

easier to implement when compared to other methods such as lock-in thermography [69, 70]. Further details are given in the following sections.

Methods

Welded joint samples were used this study because of their well-defined mapping of residual stress. The central region contains very high residual stress, while stress-free areas are at the two ends. Figure 5-1a shows the process for the sample preparation by first joining two 316 L steel plates together using a Tungsten Inert Gas (TIG) welding process. The plates had a 37-degree bevel and were 15 mm thick. The welding was done with a current of 100 A and the inert gas was argon with a 10 L/min flowrate. After this, the samples were cut using a wire electrodischarge machining process from the welded plate into samples of a thickness of 1.5 mm. The samples were then manual polished to ensure a smooth surface absent of most surface defects. Due to the reflectivity of the final polished samples, they were then coated in a thin 0.07 mm thick adhesive backed graphite coating. This was done to ensure that the IR microscope would be able to achieve an accurate surface temperature reading. The thin coating was applied uniformly across the entirety of the sample and contained no obvious surface defects.

Sample temperature was measured with an Optris PI 640 thermal microscope with 640x480 resolution focal plane array with 25 μm pixel size. It has a temperature range of -20℃ to 900℃, with a spectral range from 8 to 14 μm. The microscope also utilizes a proprietary thermography software to record and display thermal images and videos. The samples were resistively heated to a uniform temperature using an Agilent DC Power Supply, capable of up to 17A or 200V. The experimental setup is shown in Figure 5-1b.

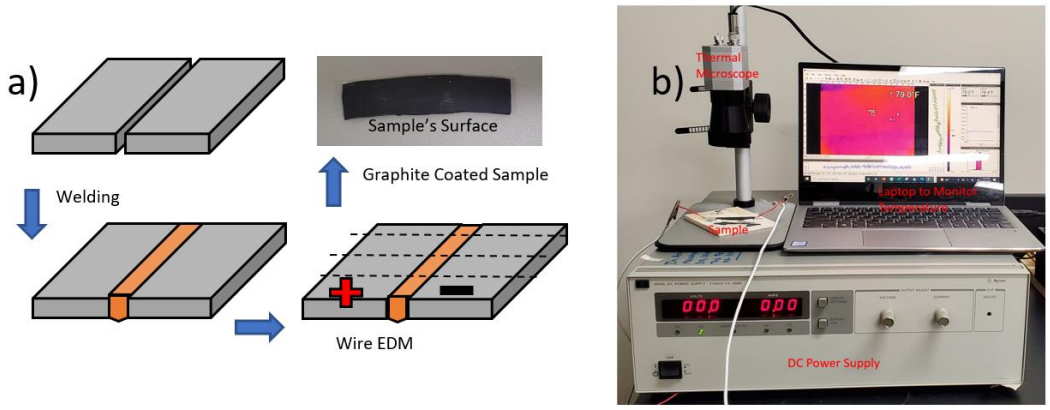

Figure 5-1. (a) Specimen preparation process. (b) Experimental set up showing the thermal camera and the DC power supply.

In a typical experiment, the sample is heated using the power supply until the temperature distribution across the entire sample is uniform and constant. In this experiment, this was achieved around 75-80 °C. Figure 1b shows the thermal image of the sample at the equilibrium temperature. As can be seen in the image the temperature is nearly uniform across the entire surface of the sample, with no more than 1℃ of variation at any two points. It is imperative that the sample is heated uniformly due to the non-linear nature of cooling, otherwise comparing the cooling rates at different points on the sample would not be accurate. The equilibrium temperature will vary based on the power being passed into the sample, but it is important that it is high enough above ambient temperatures for the different temperatures in cooling rates to be apparent, which seems to be roughly 20°C above ambient. After holding on to this temperature for 30 seconds, the power supply was turned off and the IR microscope began recording the surface temperature of the sample. The IR microscope recorded the surface temperature of the specimen at a sampling rate of 20 frames per second for the next 100 seconds. The data from the image frames is then exported as .csv file to be run through a MATLAB program to determine the cooling rates at each pixel in the frame.

The data from the thermal images are run through a MATLAB program to calculate the pixel-by-pixel cooling rate. Rather than determining a gradient across the entire several hundred frame dataset, a simpler method is employed. Since the specimen is at a uniform temperature at the start of cooling, data from the first frame, and data from the last frame (at the end of the cooling) are used to establish a linearized cooling rate, by relating the change in temperature to the timespan. This linearized cooling rate is then calculated at each pixel of the image dataset. This new data is then used to create a contour plot comparing the linearized cooling rate at each pixel. Figure 5-2 is a flowchart showing how the details of the algorithm

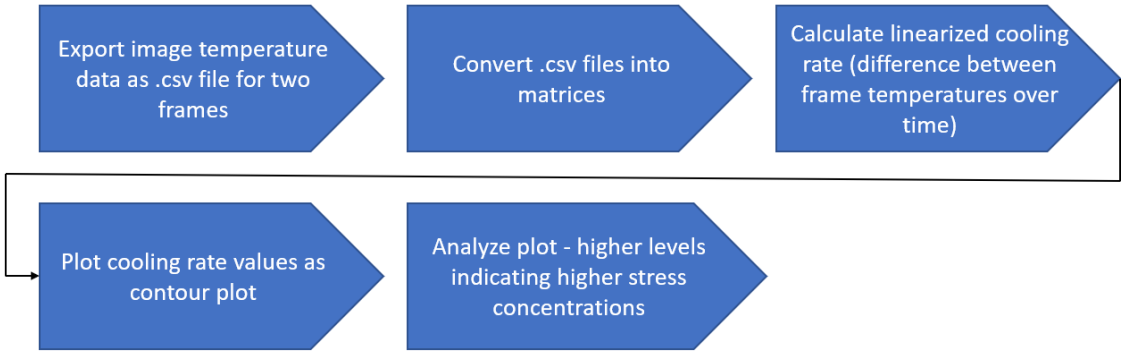

Figure 5-2: Flowchart of how the MATLAB algorithm works and is used. This flowchart begins after the thermal image data has already been taken, when the algorithm is used.

Experimental Results

As a first step towards demonstration of the proposed technique, we performed residual stress mapping of the specimens using x-ray diffraction [71] and microhardness techniques. This is a critical step because a convincing validation would require close agreement between these techniques. Figure 5-3a shows the x-ray diffraction measurement at the center of the specimen, where the residual stress is measured to be around 440 MPa. A Malvern Panalytical X'Pert 3 MRD system with 4 -circle goniometer was used to apply the sine squared psi technique [72]. Here, we scan over a particular peak for different tilt positions to meet the Bragg condition, while noting the shift of the peak. We fit a straight line is fitted to these peak positions and use the slope, the Young's modulus and the Poisson's ration to determine the residual stress. The technique is surface sensitive, hence depth of penetration, angle for Bragg criteria, and the wavelength of the radiation are important. We used Cr radiation with 2.28973 A wavelength in this study.

The microhardness technique was used to obtain a two-dimensional map of the residual stress in the specimen. We used a Qness Q60 A+ micro indenter to perform indentations along a line that spans the un-stress parent metals as well as the weld zone. It is

expected that the weld region will have very high density of immobile dislocation networks that increase hardness. This is shown in Figure 5-3b, where the weld zone has an average microhardness of 350 HV, which decreases to approximately 200 HV at the parent metal.

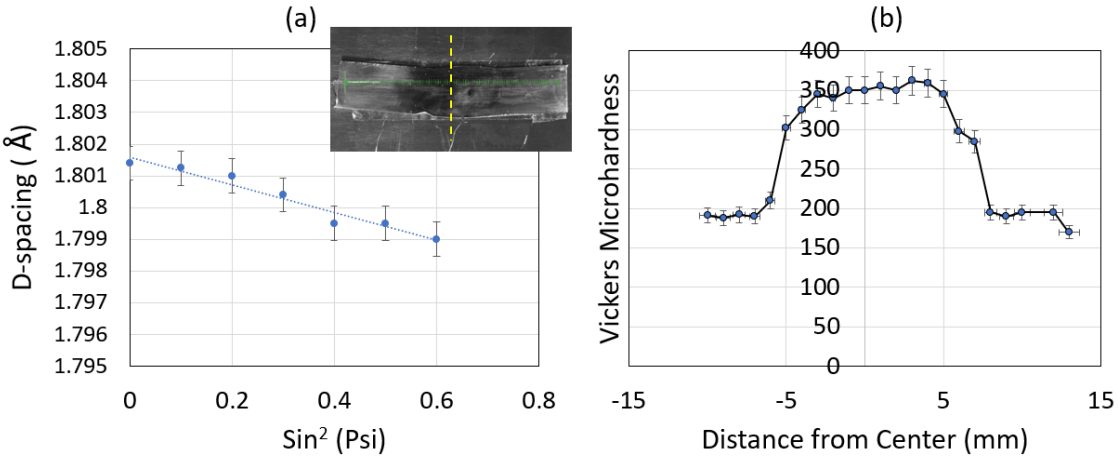

Figure 5-3: (a) X-ray diffraction measurement of residual stress at a point on the centerline (dashed line) of the specimen (b) Vickers microhardness measurement along the specimen length (green line) showing the hardness differences in the parent metal and the weld zone.

After quantifying and mapping the residual stress in the specimens, we now applying the proposed pixel by pixel cooling rate measurement technique. A representative set of results is shown in Figure 5-4. Here, clearly discernible contrast is seen in the two-dimensional cooling rate map, when we compare the central region (weld zone at 440 MPa residual stress) to the parent metal. Qualitatively, the difference between the colors in the figure correlates to a difference in residual stress concentrations. Quantitatively, we are estimating a resolution of around 42 MPa, based on the thermal camera's 0.1 °C resolution and the difference in stress between the center of the sample (Figure 5-4b, point 1) and the far edge (Figure 5-4b, point 2) being 250 MPa. With an absolute difference in the cooling rate between these two sections being 0.6 °C/s, and a temperature resolution of 0.1 °C/s, this leads to a residual stress resolution of 32 MPa with spatial resolution about 25 μm. In comparison,

the residual stress and spatial resolution for Xray diffraction is about 14 MPa and 1 mm. It is important to note that our reported resolution is for a cheaper, un-cooled infrared microscope. Therefore, significant room for improvement exists for microscopes that more precision in temperature and spatial domains.

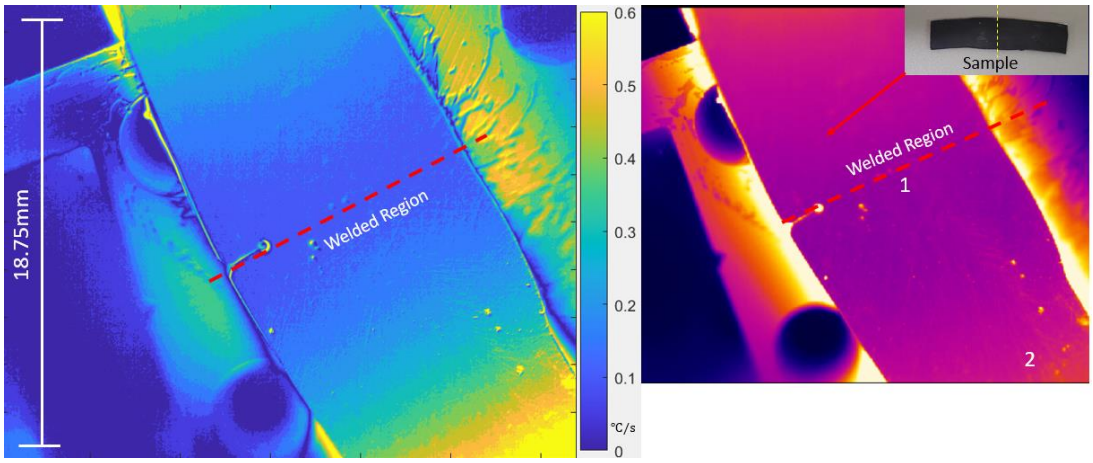

Figure 5-4: (a) Contour plot showing the difference in cooling rates on different sections of the welded sample. The color bar represents the change in temperature per second. (b) Thermal image of the sample at the onset of cooling, highlighting the uniform temperature distribution.

To explain the observed difference in cooling rate, we consider the three-dimensional heat transfer equation given below. The cooling rate is represented by the $\frac{\partial T}{\partial t}$ term, which depends on k, c_p and ρ representing the thermal conductivity, specific heat and density respectively, with the partial differentials on the left representing the temperature distribution across the specimen in three dimensions.

$$\frac{\partial}{\partial x}\left(k\frac{\partial T}{\partial x}\right)+\frac{\partial}{\partial y}\left(k\frac{\partial T}{\partial y}\right)+\frac{\partial}{\partial z}\left(k\frac{\partial T}{\partial z}\right)+q_V=\rho c_p\frac{\partial T}{\partial t} \quad (1)$$

Generally, in finite element simulations on residual stresses in welds, these properties are assumed to be the same for the welded/heat affected regions and the surrounding parent material, but this is not the case, as has been shown in the literature [73]. We can assume that the density of the welded region is very similar to that of the parent material, because 316L

filler material was used in the welding process, with 316L being the parent material. It has been shown that the thermal conductivity and specific of the welded region decreases compared to that of the parent material. It should be noted that these changes are at temperatures below 200 ℃, and the differences can vary more at higher temperatures. For temperatures below 200 ℃ (our experiments are performed at about 80 ℃), thermal conductivity decreases more rapidly than the specific heat [73]. Rearranging the nonlinear 3D heat transfer equation to solve for the rate of temperature change, we can visually inspect how the thermal conductivity and specific heat will influence the rate of temperature change.

Since we are measuring cooling rate pixel by pixel for a sample with uniform initial temperature condition, the dominating factor is the heat flow from the interior to the surface, where the heat is removed by convection. For two extremes, we consider two pixels at the weld region and parent metal. The pixel at the parent metal with higher thermal conductivity will transport more heat energy to the surface that will cool faster compared to the pixel on the weld region. The inverse effect is expected for the specific heat variation from parent metal to the weld zone. Therefore, our experimental results on slower cooling rate in the weld zone agrees with the study that thermal conductivity will decrease by a larger factor than the specific heat at temperatures under 200 ℃ [73].

Conclusion

Nondestructive evaluation techniques are critical for commercial and industrial applications, where production parts need to be tested without being damaged. In most cases, particularly for residual stress measurement, these techniques are mostly relegated to research environments due to their complexity and difficulty to implement. For example, the Xray diffraction technique is impractical to be directly applied to a welded joint. Another well-established technique, ultrasonic testing also required special medium that can hinder in-operando testing of systems or components. To address this concern, we present a simpler thermal imaging-based technique that can estimate the residual stress. The basic requirement is smooth and contaminant free surface and line of sight to an infrared camera. The region of interest is heated to uniform temperature and then cooled by natural convection. The cooling rate is compared with the same material with no known residual stress. The fundamental mechanics is that higher residual stresses involve higher concentrations of microstructural defects that decrease the thermal conductivity of a material. For uniform initial temperature condition, this decrease in the thermal conductivity causes the material to have a slower cooling rate. We have demonstrated this mechanism on welded 316 steel samples. With cheap, uncooled thermal camera, we report residual stress resolution of about 32 MPa and spatial resolution of 25 μm. This compares favorably with x-ray diffraction technique with corresponding values of 14 MPa and about 1 mm. However, the unique advantage of our approach is its applicability on systems and components and not just in laboratory setup. Future work may be focused on increasing the resolution of this method and further increasing the ease of implementation.

Chapter 5

Conclusion

Shape memory alloys are a functional material whose unique properties allow them to be useful as solid-state actuators. These properties, known as shape memory properties, allow the material to recover large amounts of strain, on occasion over 6%. Despite being unique, the shape memory properties are often not great enough for SMAs to be used as actuators in some applications. Improving these shape memory properties is key to expanding possible applications of shape memory alloys. The first focus of this thesis was on improving the actuation rate of SMAs through novel actuation methods.

The first method explored was segmented actuation, which resulted in an improvement in the actuation frequency of 24%. Following the segmented actuation experiments, a method referred to in this paper as Frequency Optimized Segmented Actuation was developed. FOSA was able to improve the actuation frequency an additional 86%; however, there were some limitations to this method, with the primary issue being that the recoverable strain is decreased by 50% in order to achieve the high actuation speed. The decrease in recoverable strain is a result of the method restricting a full martensitic transformation in the material. This issue of the recoverable strain decreasing led to the remainder of this research being focused towards increasing the recoverable strain.

The recoverable strain of the material was improved in this research through a novel method of heat treatment, known as Electropulse Aging Treatment. EAT is a method of near room-temperature heat treatment which results in improved shape memory properties. It was found that by using EAT at 100A, with a pulse width of 4ms and a frequency of 2Hz, the recoverable strain of the SMA can be increased from 5% to roughly 7%. This improvement was

by a possible reduction in defects inside the material, which was investigated using XRD and DSC methods. However, it was thought that further increasing the current amplitude may lead to further improvements in shape memory properties, which was a limitation of the available equipment.

Towards the end of the research conducted in this thesis, our lab group obtained the Eagle Harbor Power Module, which was able to achieve currents as high as 6000A. This higher current was an improvement over the 100A of our older equipment. Though the new equipment was not able to be used to its full potential by the end of this research, some interesting results had already been obtained. It was found that by increasing the current to 1000A, there were no additional gains in the recoverable strain; however, there were changes in the characteristic temperatures of the material, specifically a moving of the M_s and A_f temperatures closer together, which in theory may lead to improved actuation rates.

The original focus of this research was on improving shape memory alloys in a way that they would make better actuators. This was first done by working on improving the actuation rates of standard NiTi alloys, which was achieved at the cost of the recoverable strain. The recoverable strain was then improved through electropulse aging treatment, which has some potential to influence phase transformation temperatures at higher current amplitudes. These methods can be combined to result in an overall net improvement of shape memory alloys in actuator applications, specifically those in which high actuation rates are required without sacrificing strength (useful load).

Future work will need to be focused on trying new combinations of electropulsing parameters in attempt to further improve shape memory properties. Other types of shape memory alloys may also be tried in this process, such as Fe based SMAs, which tend to be more defect heavy. It is also important that the changes in the microstructure from the EAT process are better characterized and understood, either through current XRD and DSC methods, or other processes.

Appendix

Materials

The primary SMA material used in these studies was a commercial NiTi SMA manufactured by Kellogg's Research Labs. The NiTi was purchased in wire form, generally in short lengths of 5 feet. This wire was cold drawn through a circular die and was heat treated by the manufacturer. The surface of the material was uncoated and polished by the manufacturer. The wire is available in a number of different actuation temperature ratings, which refers to the A_f temperature of the material. The temperatures available were Super Elastic (10C), Air Temp (20C), Body Temp (35C), Standard Temp (45C), and High Temp (80C). The focus of this work is on the Shape Memory Effect rather than the Super Elastic, so the Super Elastic wire was not considered. Because the High Temp wire resulted in the fastest actuation time, it was selected for the majority of the testing.

The SMA wire was also available in a variety of diameters. The diameters which were available to us were 75-micron, 250-micron, 500-micron, 1mm, and 2mm diameter wires. These diameters were available in all the temperature ratings. Original work on this project began with the 2mm diameter SMA wire, however as the work progressed the diameter of the wire was slowly reduced, with all of them being tested at some point.

Experimental Testing Set Ups

Displacement Testing Set Up

In order to measure the recoverable strain of the SMA wires, it was necessary to create an experimental set up that would allow us to measure the displacement of the SMA wire during actuation. This actuation of the wire requires hanging a load from the SMA wire, which can be as heavy as 20Kg for 2mm diameter wires. Therefore, it is imperative that the testing set up is not only strong enough to hold the load, but strong enough to not flex during the actuation of the load to ensure accurate measurements. Two iterations of this testing set up were required to meet these needs. Originally, the displacement of the SMA wires during actuation was measured by actuating the wire in a testing rig constructed from 1" black steel pipe with some additional 1.5" SCH40 PVC fittings. The grippers were constructed from eSUN PLA+, which was 3D printed for each specific SMA wire diameter. The testing set up had issues with flexing under load, due to the small base. 3D printed grippers should be avoided for SMA or any thin wires.

The next iteration of the testing set up was created to address the issue of excessive flexing under load. This testing set up can be seen in Figure 1, created using 1.5" aluminum extrusion pieces. The length of the testing rig allows for 50cm of SMA wire to be actuated at once. The SMA wire also rests on a pulley, to ensure that friction is not inhibiting the actuation of the wire. Since the base of the testing rig is large, and a considerable amount of aluminum is used, there is zero flexing under load. An additional area of concern from the previous version was the 3D printed grips. These grips would wear quickly, and if used enough would slip, thereby dropping the load. The slipping issue in the grips resulted in a safety issue since the loads were often heavy, so the grippers were upgraded to tensile testing grippers. The improved grippers are able to secure any available diameter of SMA wire.

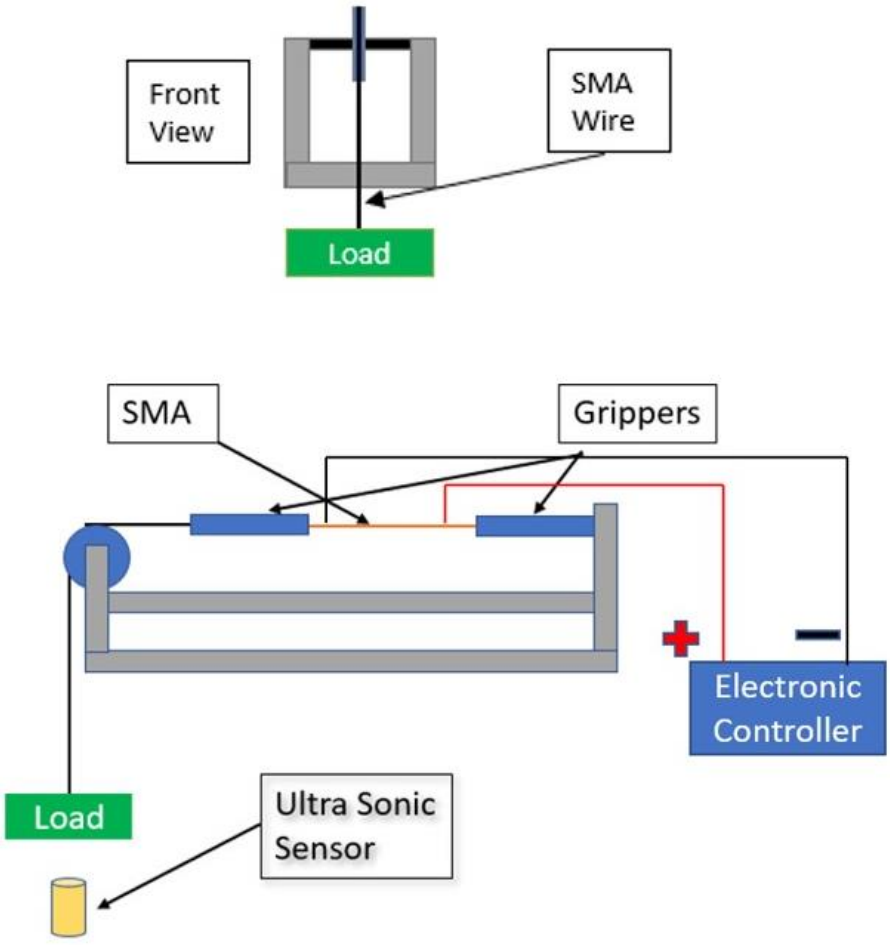

Figure A-1: Displacement Testing Jig.

Arduino Displacement Sensor and Controller

Displacement Sensor

In order to characterize the recoverable strain of the SMA, the displacement of the sample during actuation needed to be measured. To do this, an Arduino board and an ultra-sonic sensor were incorporated into the displacement testing set up. The Arduino board was an Arduino uno, manufactured by Elegoo. This board had a HC-SR04 utlrasonic sensor wired to it, which was used to measure the recoverable strain. The sensor could reliably measure the displacement

during actuation to +/- 1mm. This was sufficient to get good data for actuations over 15mm, which correlates to a wire length of at least 25cm.

Figure A-2 shows the wiring diagram of the Arduino board and the ultrasonic sensor. The red wire represents a connection between the 5V output pin on the Arduino and the 5V input pin on the sensor. For the ground pins on both, the black wire is used, with the blue and yellow wires representing a connection of pins 11 and 12 with the echo and trigger pins on the sensor, respectively. To receive power, the board was also connected to a laptop using a Type-A USB cable, which also provided data transfer. A script was written in the Ardino development environment (IDE) which controlled and recorded sensor data. The script allowed for two parameters to be changed; the resolution, which could be changed between a millimeter and a centimeter, and the sampling frequency. The sampling frequency was set to 4 Hz due to the slow speed of SMA actuation. However, during the faster actuation of thinner wires the frequency was increased. It should be noted that the wiring diagram shown in Figure A-2 is representative of the actual wiring in the experimental set up, so if the same code is used the sensor will work. However if a different Arduino script is used, the pin callouts may need to be adjusted in the script for this specific wiring diagram to work.

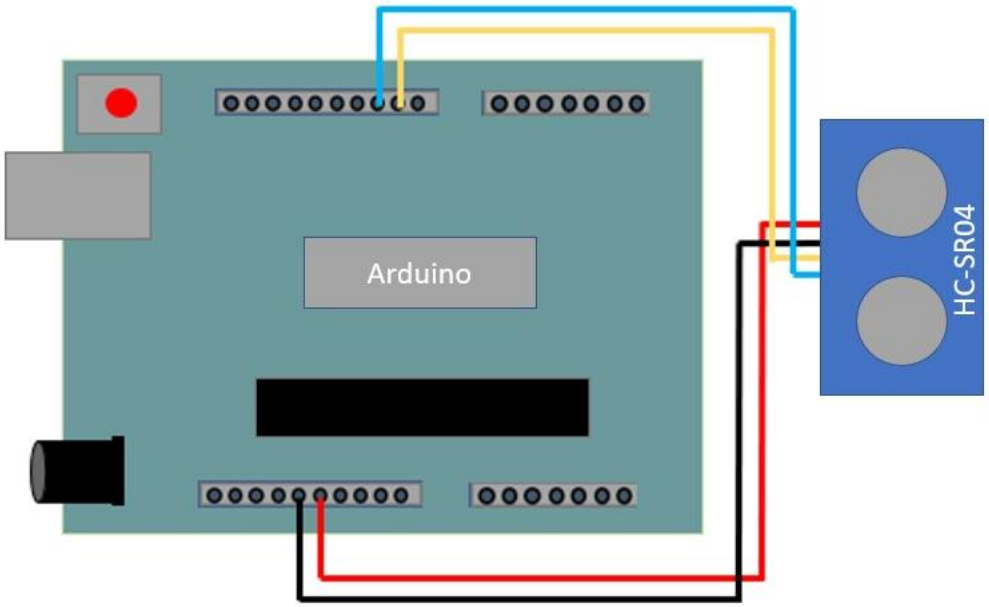

Figure A-2: Wiring diagram for Arduino based ultrasonic sensor.

Arduino Controller

To actuate the SMAs, a power supply was used to pass DC current through the alloy, therefore heating it. Because the power supply could not quickly turn on and off, high frequency actuation experiments were difficult. To get around this, a controller was made using an Arduino. The purpose of this controller was to give precise control of when and where power from the DC supply was being sent. The controller was based on an Arudino uno manufactured by Elegoo and an 8-channel relay, which could send power to multiple SMA wires. A script was written for this controller, with the following parameters: the duration of time the power is being sent, and the SMA (or relay channel) which the power is being sent. A wiring diagram for the controller can be seen in Figure 2

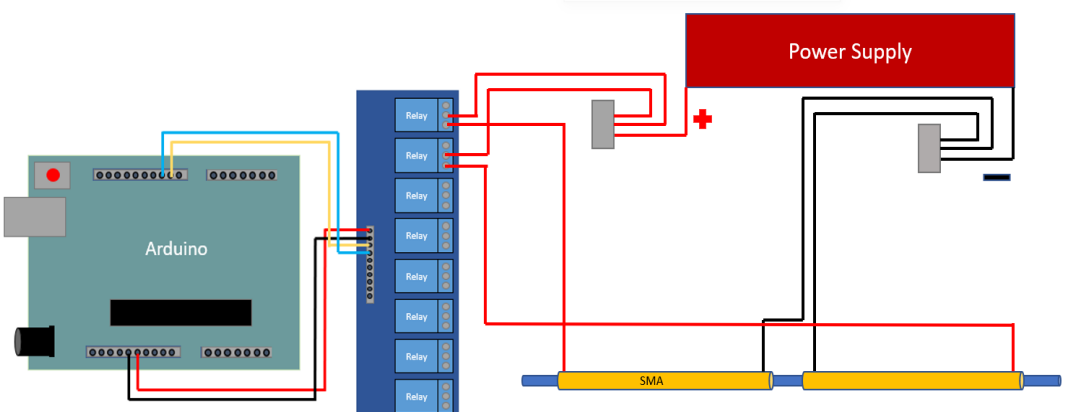

Figure A-3: Wiring diagram for Arduino based controller.

Thermal Camera

Throughout this research a thermal camera was used to monitor the surface temperature of the SMA during actuation. Due to the temperature dependence of actuation, accurately measuring this temperature was important to properly characterize the samples. To do this, an Optris PI640 thermal camera was used, which boasts a high resolution of 640x480p. In addition to the high resolution, the sensor was capable to up to 32 frames per second with the ability to accurately measure the temperature to the nearest tenth of a degree. Temperature and time data were exported for each pixel of each frame in order to properly analyze the data from the camera. Optris also has a proprietary software for this camera, the Optris PIX Connect, which has real time monitoring and recording of the thermal data.

It should be noted that the proprietary software can be downloaded one of two ways; either through the manufacturer's website, or the Optris USB drive in the lab. One common issue that may be encountered when first using the PIX software is a black screen where the thermal output image should be. This can be solved by going into the following tab: Tools > Configuration > General. In the general tab there should be a slide bar that allows you to chose between performance and quality, set it to the center and the camera should begin to work.

Eagle Harbor Electropulser

Used in some experiments towards the end of this research, the Eagle Harbor Electropulser allows for pulsing with current in excess of 6000A. This pulser set up is similar to the previous set up, however has some key differences. This pulser has a dedicated pulser that is powered by a DC power supply (Magna 575), however this DC power supply is capable of 600V. The Eagle Harbor Power Unit (the pulser), does not have controls for frequency, amplitude, or pulse width as the Northrop unit does. For this set up, the frequency and pulse width parameters are controlled by the BNC Signal Generator.

The signal generator can be seen in figure A-4, and controls the frequency and pulse width of the signal. The pulse width can range from several seconds down to nanoseconds. The frequency ranges from 0.1 Hz to 1000 Hz. This signal generator is attached to the Eagle Harbor Power Unit with a fiber optic cable, and it is important that the signal generator is kept at least 10' away from the power unit due to shielding issues. The run stop button on the signal generator is what controls whether or not the Eagle Harbor Power Unit is sending pulses of current or not, it is the primary switch to be used when pulsing samples. Between the signal generator and the power unit is the FT-1, a device which connects the signal generators output and converts it into a signal which can be fed through the fiber optic cable. It is imperative that the FT-1 is plugged into a power source before a signal is sent through, or it could be damaged.

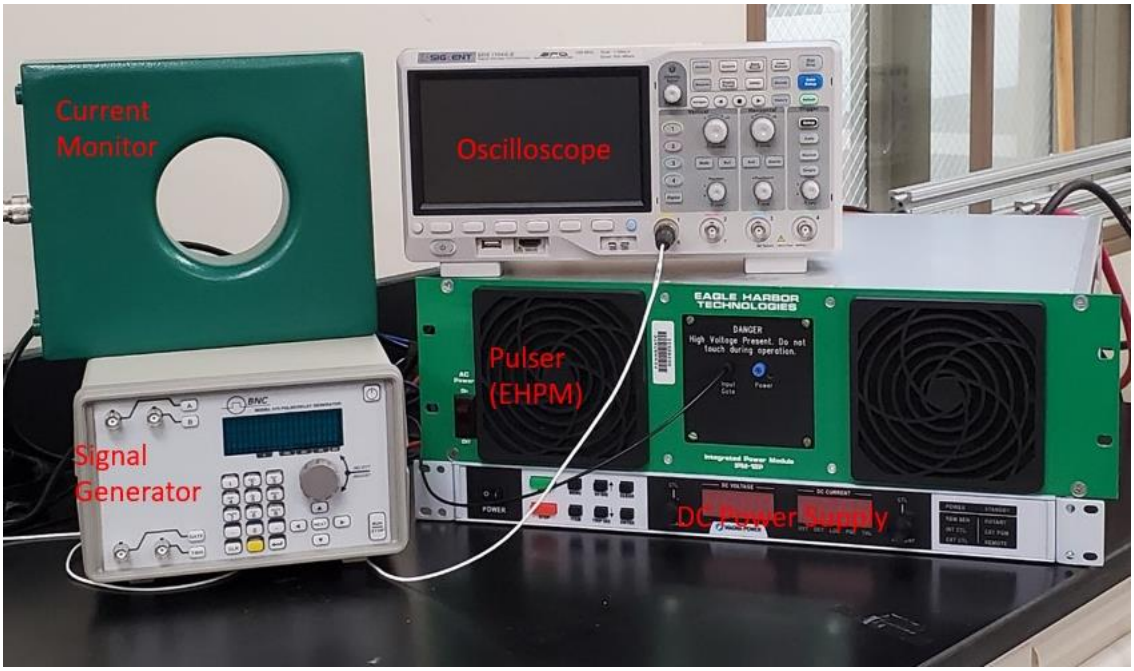

Figure A-4: Eagle Harbor Power Module and equipment.

The DC power supply is what powers the Eagle Harbor Power Unit. The device is turned on by the power switch, as shown in figure A-4, however it will not send power until the green start button is pushed. Pushing the red stop button will stop power delivery. The power being delivered is generally controlled by the voltage knob, and can range from 0-600V. However, the current knob must be turned one full rotation before the voltage knob will begin to increase the power. As shown in figure blank, the DC power supply is connected to the Eagle Harbor Power Unit's HV IN input. It will work if it is connected to any two HV IN pins, regardless of where the power unit's output is connected to.

The Eagle Harbor Power unit has two switches, one located in the back, and one located in the front. The one in the back should be turned on first, then the one in the front. It is important that the output pins are properly grounded using the "chicken stick" before the rear switch is turned off, as there are high voltage outputs along the back of the power unit. Figure A-5 shows the outputs on the back of the power unit. For the output to work, wires must be connected to two

positive HV Out and two negative HV Out pins. These wires are then connected together before they are attached to the sample. These wires can be attached to any combination of output pins, as long as it uses four total output pins, and two are positive and two are negative. Due to the high currents involved with this equipment, it is important that these outputs are not touched without proper precautions. According to the manufacturer, allow several minutes to pass after use for the capacitors inside the pulser to discharge. Then use the chicken stick (in the lab), to ensure capacitors have discharger. Finally, use a multimeter to ensure there is no more power being sent to the outputs.

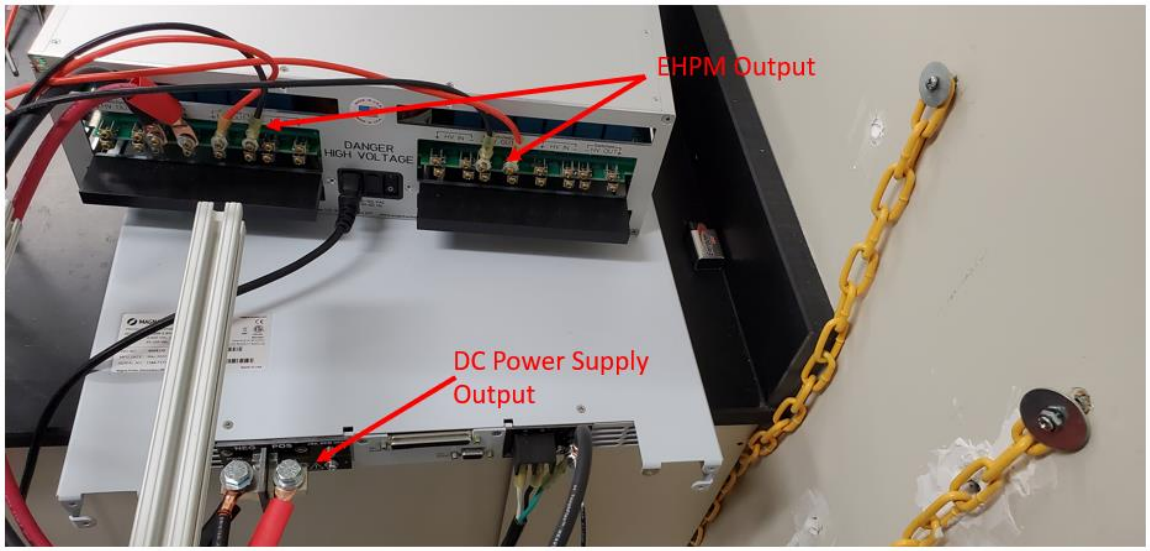

Figure A-5: Eagle Harbor Power Module and DC power supply outputs.

Unlike the Northrop pulser, there is no means to set the current on the Eagle Harbor equipment. Rather, the current can be measured using the current monitor connected to an oscilloscope. The output current is the voltage amplitude recorded by the current monitor multiplied by 40. Therefore, an output on the oscilloscope of 10V would be 400A. The current can be varied by the frequency and pulse width settings on the signal generator, as well as by

increasing the voltage supply. Increasing the pulse width and decreasing the frequency generally results in an increase in the current amplitude. However, it is important to start at a low voltage and pulse width for a new sample because the current output will be unknown. Too high parameters will result in arcing across the sample which may damage the sample.

There are other safety recommendations when using this equipment. One is that the sample and all other wires should be taped down to the table before use, this is especially important for SMAs which may move during pulsing. If the wires or samples move a short may be created, which may be particularly loud at these high currents. Another safety option is to use the thick rubber gloves in the lab when removing samples, as these are insulated. Additionally, insulated tools should be used when working on the equipment; however, most tools in the lab should already fit this criteria. The most important tip with this equipment is to always start low and slow with the current, and then progressively increase the current in small intervals. This will ensure the best results experimentally while also keeping the lab safe.

Bibliography

[1] Duerig, T., Pelton, A., & Stöckel, D. (1999). An overview of nitinol medical applications. *Materials Science and Engineering A*, *273–275*.

[2] Barras, C. D. J., & Myers, K. A. (2000). Nitinol - Its use in vascular surgery and other applications. In *European Journal of Vascular and Endovascular Surgery* (Vol. 19, Issue 6). https://doi.org/10.1053/ejvs.2000.1111

[3] Wu, Y., Zhang, Y., Xi, J., Li, M.-J., & Li, X. (2010). Fiber-optic nonlinear endomicroscopy with focus scanning by using shape memory alloy actuation. *Journal of Biomedical Optics*, *15*(6).

[4] Le, V. H., Hernando, L. R., Lee, C., Choi, H., Jin, Z., Nguyen, K. T., Go, G., Ko, S. Y., Park, J. O., & Park, S. (2015). Shape memory alloy-based biopsy device for active locomotive intestinal capsule endoscope. *Proceedings of the Institution of Mechanical Engineers, Part H: Journal of Engineering in Medicine*, *229*(3).

[5] Soul, H., & Yawny, A. (2017). Applicability of superelastic materials in seismic protection systems: A parametric study of performance in isolation of structures. *Smart Materials and Structures*, *26*(8).

[6] González-Sanz, G., Galé-Lamuela, D., Escolano-Margarit, D., & Benavent-Climent, A. (2019). Hysteretic behavior and ultimate energy dissipation capacity of large diameter bars made of shape memory alloys under seismic loadings. *Metals*, *9*(10).

[7] Zhang, C. Y., Tian, F. Y., & Ni, X. D. (2020). First-principles investigation on ideal strength of B2 NiAl and NiTi alloys. *Chinese Physics B*, *29*(3).

[8] Bhattacharya, K., & Kohn, R. v. (1996). Symmetry, texture and the recoverable strain of shape-memory polycrystals. *Acta Materialia*, *44*(2).

[9] Ashrafi, M. J. (2019). Constitutive modeling of shape memory alloys under cyclic loading considering permanent strain effects. *Mechanics of Materials*, *129*.

[10] McKelvey, A. L., & Ritchie, R. O. (2001). Fatigue-crack growth behavior in the superelastic and shape-memory alloy nitinol. *Metallurgical and Materials Transactions A: Physical Metallurgy and Materials Science*, *32*(13).

[11] Saud, S. N., Hamzah, E., Abubakar, T., Ibrahim, M. K., & Bahador, A. (2015). Effect of a fourth alloying element on the microstructure and mechanical properties of Cu-Al-Ni shape memory alloys. *Journal of Materials Research*, *30*(14).

[12] Hong, K. N., Yeon, Y. M., Shim, W. B., & Ji, S. W. (2020). Fatigue characteristics of Fe-based shape-memory alloys. *Applied Sciences (Switzerland)*, *10*(17).

[13] Liang, C., & Rogers, C. A. (1990). One-Dimensional Thermomechanical Constitutive Relations for Shape Memory Materials. *Journal of Intelligent Material Systems and Structures*, *1*(2).

[14] Boyd, J. G., & Lagoudas, D. C. (1996). A thermodynamical constitutive model for shape memory materials. Part I. The monolithic shape memory alloy. *International Journal of Plasticity*, *12*(6).

[15] Morawiec, H., Stróz, D., & Chrobak, D. (1995). Effect of Deformation and Thermal Treatment of NiTi Alloy on Transition Sequence. *Le Journal de Physique IV*, *05*(C2).

[16] Xue, D., Xue, D., Yuan, R., Zhou, Y., Balachandran, P. v., Ding, X., Sun, J., & Lookman, T. (2017). An informatics approach to transformation temperatures of NiTi-based shape memory alloys. *Acta Materialia*, *125*.

[17] Frenzel, J., George, E. P., Dlouhy, A., Somsen, C., Wagner, M. F. X., & Eggeler, G. (2010). Influence of Ni on martensitic phase transformations in NiTi shape memory alloys. *Acta Materialia*, *58*(9).

[18] Zhang, Y., & Xu, X. (2020). Transformation Temperature Predictions Through Computational Intelligence for NiTi-Based Shape Memory Alloys. *Shape Memory and Superelasticity*, *6*(4).

[19] Shaw, J. A., & Kyriakides, S. (1995). Thermomechanical aspects of NiTi. *Journal of the Mechanics and Physics of Solids*, *43*(8), 1243–1281.

[20] Frost, M., Jury, A., Heller, L., & Sedlák, P. (2021). Experimentally validated constitutive model for NiTi-based shape memory alloys featuring intermediate R-phase transformation: A case study of Ni48Ti49Fe3. *Materials and Design*, *203*.

[21] Copaci, D. S., Blanco, D., Martin-Clemente, A., & Moreno, L. (2020). Flexible shape memory alloy actuators for soft robotics: Modelling and control. *International Journal of Advanced Robotic Systems*, *17*(1).

[22] Eggeler, G., Hornbogen, E., Yawny, A., Heckmann, A., & Wagner, M. (2004). Structural and functional fatigue of NiTi shape memory alloys. *Materials Science and Engineering A*, *378*(1-2 SPEC. ISS.).

[23] Shi, F., Ozbulut, O. E., Li, Z., Wu, Z., Ren, F., & Zhou, Y. (2022). Effects of ambient temperature on cyclic response and functional fatigue of shape memory alloy cables. *Journal of Building Engineering*, *52*.

[24] Soother, D. K., Daudpoto, J., & Chowdhry, B. S. (2020). Challenges for practical applications of shape memory alloy actuators. In *Materials Research Express* (Vol. 7, Issue 7).

[25] Saedi, S., Turabi, A. S., Andani, M. T., Haberland, C., Karaca, H., & Elahinia, M. (2016). The influence of heat treatment on the thermomechanical response of Ni-rich NiTi alloys manufactured by selective laser melting. *Journal of Alloys and Compounds*, *677*.

[26] Paula, A. S., Canejo, J. P. H. G., Martins, R. M. S., & Braz Fernandes, F. M. (2004). Effect of thermal cycling on the transformation temperature ranges of a Ni-Ti shape memory alloy. *Materials Science and Engineering A*, *378*(1-2 SPEC. ISS.).

[27] Gao, W., Yi, X., Song, G., Wang, Z., & Meng, X. (2020). Zr50Cu25Ni7.5Co17.5 high-temperature shape memory alloy with excellent thermal stability and large recovery strain, and the associated microstructural deformation mechanism. *Materials and Design*, *196*.

[28] Saud, S. N., Hamzah, E., Abubakar, T., Ibrahim, M. K., & Bahador, A. (2015). Effect of a fourth alloying element on the microstructure and mechanical properties of Cu-Al-Ni shape memory alloys. *Journal of Materials Research*, *30*(14). https://doi.org/10.1557/jmr.2015.196

[29] Huang, X., & Liu, Y. (2001). Effect of annealing on the transformation behavior and superelasticity of NiTi shape memory alloy. *Scripta Materialia*, *45*(2).

[30] Lohan, N.-M., Toma, Ç.-L., Popa, M., Cazac, A. M., & Pricop, B. (2021). Influence of alloying elements on the thermal behavior of NiTi shape memory alloys. *MATEC Web of Conferences*, *342*. https://doi.org/10.1051/matecconf/202134206007

[31] Salvetr, P., Školáková, A., Šulcová, L., Kačenka, Z., Kadlecová, B., & Novák, P. (2018). Effect of zirconium, niobium and chromium on structure and properties of Ni-Ti alloy. *Manufacturing Technology*, *18*(5).

[32] Motzki, P., Gorges, T., Kappel, M., Schmidt, M., Rizzello, G., & Seelecke, S. (2018). High-speed and high-efficiency shape memory alloy actuation. *Smart Materials and Structures*, *27*(7).

[33] Simone, F., York, A., & Seelecke, S. (2015). Design and fabrication of a three-finger prosthetic hand using SMA muscle wires. *Bioinspiration, Biomimetics, and Bioreplication 2015*, *9429*.

[34] Song, S. H., Lee, J. Y., Rodrigue, H., Choi, I. S., Kang, Y. J., & Ahn, S. H. (2016). 35 Hz shape memory alloy actuator with bending-twisting mode. *Scientific Reports*, *6*.

[35] Abdullah, E. J., Soriano, J., Fernández de Bastida Garrido, I., & Abdul Majid, D. L. (2021). Accurate position control of shape memory alloy actuation using displacement feedback and self-sensing system. *Microsystem Technologies*, *27*(7).

[36] Brailovski, V., Terriault, P., & Prokoshkin, S. (2002). Influence of the post-deformation annealing heat treatment on the low-cycle fatigue of NiTi shape memory alloys. *Journal of Materials Engineering and Performance*, *11*(6).

[37] Brailovski, V., Terriault, P., & Prokoshkin, S. (2002). Influence of the post-deformation annealing heat treatment on the low-cycle fatigue of NiTi shape memory alloys. *Journal of Materials Engineering and Performance*, *11*(6).

[38] Motemani, Y., Nili-Ahmadabadi, M., Tan, M. J., Bornapour, M., & Rayagan, S. (2009). Effect of cooling rate on the phase transformation behavior and mechanical properties of Ni-rich NiTi shape memory alloy. *Journal of Alloys and Compounds*, *469*(1–2).

[39] Jayachandran, S., Akash, K., Mani Prabu, S. S., Manikandan, M., Muralidharan, M., Brolin, A., & Palani, I. A. (2019). Investigations on performance viability of NiTi, NiTiCu, CuAlNi and CuAlNiMn shape memory alloy/Kapton composite thin film for actuator application. *Composites Part B: Engineering*, *176*.

[40] Prokoshkin, S. D., Brailovski, V., Inaekyan, K. E., Demers, V., Khmelevskaya, I. Y., Dobatkin, S. v., & Tatyanin, E. v. (2008). Structure and properties of severely cold-rolled and annealed Ti-Ni shape memory alloys. *Materials Science and Engineering A*, *481–482*(1-2 C).

[41] Hua, P., Xia, M., Onuki, Y., & Sun, Q. (2021). Nanocomposite NiTi shape memory alloy with high strength and fatigue resistance. *Nature Nanotechnology*, *16*(4).

[42] Follador, Maurizio & Cianchetti, Matteo & Arienti, Andrea & Laschi, Cecilia. (2012). A general method for the design and fabrication of shape memory alloy active spring actuators. Smart Materials and Structures. 21.

[43] Kumar, N., Mishra, R. S., & Baumann, J. A. (2014). Introduction. In N. Kumar, R. S. Mishra, & J. A. Baumann (Eds.), Residual Stresses in Friction Stir Welding (pp. 1-4). Butterworth-Heinemann, Boston.

[44] Withers, P. J., & Bhadeshia, H. K. D. H. (2001). Residual stress. Part 2 – Nature and origins. Materials Science and Technology, 17(4), 366-375.

[45] Deal, A., Spinelli, I., Chuang, A., Gao, Y., & Broderick, T. (2021). Measuring residual stress in Ti-6Al-4V with HR-EBSD, using reference patterns from annealed material. Materials Characterization, 175, 111027.

[46] McClung, R. C. (2007). A literature survey on the stability and significance of residual stresses during fatigue. Fatigue & Fracture of Engineering Materials & Structures, 30(3), 173-205.

[47] Li, Y., Fu, R., Li, Y., Peng, Y., & Liu, H. (2018). Abnormal Grain Growth in the Heat Affected Zone of Friction Stir Welded Joint of 32Mn-7Cr-1Mo-0.3N Steel during Post-Weld Heat Treatment. Metals, 8(4).

[48] Fuštar, B., Lukačević, I., & Dujmović, D. (2018). Review of Fatigue Assessment Methods for Welded Steel Structures. Advances in Civil Engineering, 2018, 3597356.

[49] Duan, Q., Pan, H., Fu, B., & Yan, J. (2019). An Investigation on the Strengthening Mechanism Based on Grain-Boundary Misorientation of High-Strength Pipeline Steel. steel research international, 90(12), 1900317.

[50] Hackel, L., Rankin, J., Walter, M., Dane, C. B., Neuman, W., Oneid, P., Thomas, G., & Bidrawn, F. (2019). Preventing Stress Corrosion Cracking of Spent Nuclear Fuel Dry Storage Canisters. Procedia Structural Integrity, 19, 346-361.

[51] Toda-Caraballo, I., Chao, J., Lindgren, L. E., & Capdevila, C. (2010). Effect of residual stress on recrystallization behavior of mechanically alloyed steels. Scripta Materialia, 62(1), 41-44.

[52] Jiang, W., Xie, X., Wang, T., Zhang, X., Tu, S.-T., Wang, J., & Zhao, X. (2021). Fatigue life prediction of 316L stainless steel weld joint including the role of residual stress and its evolution: Experimental and modelling. International Journal of Fatigue, 143, 105997.

[53] Sticchi, M., Schnubel, D., Kashaev, N., & Huber, N. (2015). Review of residual stress modification techniques for extending the fatigue life of metallic aircraft components. Applied Mechanics Reviews, 67(1).

[54] Guo, J., Fu, H., Pan, B., & Kang, R. (2021). Recent progress of residual stress measurement methods: A review. Chinese Journal of Aeronautics, 34(2), 54-78.

[55] Rossini, N. S., Dassisti, M., Benyounis, K. Y., & Olabi, A. G. (2012). Methods of measuring residual stresses in components. Materials & Design, 35, 572-588.

[56] Zhang, Z., Tan, Q., Cui, Y., Tian, Y., Wang, Y., Qin, H., Bi, Z., & Wang, Y. (2021). Experimental validation of residual stress thermomechanical simulation in as-quenched superalloy discs by using diffraction and incremental hole-drilling methods. Materials Today Communications, 27.

[57] Gautam, N., A.K. S., & Mondi, P. R. (2021). Evaluation methods for residual stress measurement in large components. Materials Today: Proceedings, 44, 4239-4244.

[58] Mansilla, C., Martínez-Martínez, D., Ocelík, V., & De Hosson, J. T. M. (2015). On the determination of local residual stress gradients by the slit milling method. Journal of Materials Science, 50(10), 3646- 3655.

[59] Cunha, F. G., Santos, T. G., & Xavier, J. (2021). In Situ Monitoring of Additive Manufacturing Using Digital Image Correlation: A Review. Materials, 14(6).

[60] Acevedo, R., Sedlak, P., Kolman, R., & Fredel, M. (2020). Residual stress analysis of additive manufacturing of metallic parts using ultrasonic waves: State of the art review. Journal of Materials Research and Technology, 9(4), 9457-9477.

[61] Withers, P., Turski, M., Edwards, L., Bouchard, P., & Buttle, D. (2008). Recent advances in residual stress measurement. International Journal of Pressure Vessels and Piping, 85(3), 118-127.

[62] Kruse, D., Prekel, H., Goch, G., & Walther, H. G. (2007). Correlation between hardening depth and thermal parameters based on photothermal measurements. Estonian Journal of Engineering, 13(4).

[63] Suriani, M. J., Ali, A., Khalina, A., Sapuan, S. M., & Abdullah, S. (2012). Detection of defects of Kenaf/Epoxy by Thermography Analyses. IOP Conference Series: Materials Science and Engineering, 36, 012013.

[64] Rodríguez-Martín, M., Lagüela, S., González-Aguilera, D., & Rodríguez-Gonzálvez, P. (2016). Crack-Depth Prediction in Steel Based on Cooling Rate. Advances in Materials Science and Engineering, 2016, 1016482.

[65] Robinson, A. F., Dulieu-Barton, J. M., Quinn, S., & Burguete, R. L. (2009). A review of residual stress analysis using thermoelastic techniques. Journal of Physics: Conference Series, 181, 012029.

[66] Paoloni, S., Tata, M. E., Scudieri, F., Mercuri, F., Marinelli, M., & Zammit, U. (2010). IR thermography characterization of residual stress in plastically deformed metallic components. Applied Physics A, 98(2), 461-465.

[67] Wan, Y., Jiang, W., Song, M., Huang, Y., Li, J., Sun, G., Shi, Y., Zhai, X., Zhao, X., & Ren, L. (2019). Distribution and formation mechanism of residual stress in duplex stainless steel weld joint by neutron diffraction and electron backscatter diffraction. Materials & Design, 181, 108086.

[68] van der Voort, E., & Guyot, P. (1971). On the electrical resistivity by scattering on metallic grain boundaries. physica status solidi (b), 47(2), 465-473.

[69] Chen, J., Li, K., Wang, Y., Xing, L., Yu, C., Liu, H., Ma, J., Liu, W., & Shen, Z. (2020). The effect of hot isostatic pressing on thermal conductivity of additively manufactured pure tungsten. International Journal of Refractory Metals and Hard Materials, 87, 105135.

[70] Rodríguez-Martin, M., Lagüela, S., González-Aguilera, D., & Arias, P. (2014). Cooling analysis of welded materials for crack detection using infrared thermography. Infrared Physics & Technology, 67, 547-554.

[71] Vavilov, V. P., & Burleigh, D. D. (2015). Review of pulsed thermal NDT: Physical principles, theory and data processing. NDT & E International, 73, 28-52.

[72] Matsuda, M., Okita, K., Nakagawa, T., & Sasaki, T. (2017). Application of X-ray stress measurement for residual stress analysis by inherent strain method - Comparison of cosα and $\sin^2\Psi$ method. Mechanical Engineering Journal, 4(5), 17-00022-17-00022.

[73] Haase, A., Klatt, M., Schafmeister, A., Stabenow, R., & Ortner, B. (2014). The generalized sin2ψ method: An advanced solution for X-ray stress analysis in textured materials. Powder Diffraction, 29(2), 133-136.

[74] Zhu, X. K., & Chao, Y. J. (2002). Effects of temperature-dependent material properties on welding simulation. Computers & Structures, 80(11), 967-976.